ISSN 1840-4855
e-ISSN 2233-0046

Original scientific article
http://dx.doi.org/10.70102/afts.2025.1834.732

BIOCONVECTIVE MHD SUTTERBY HYBRID NANOFLUID FLOW WITH FUZZY VOLUME FRACTION OVER A CONVECTIVELY HEATED STRETCHING SHEET

P. Asaigeethan[1*], M. Perumalsamy[2], M. Gnanakumar[3], J. Duraikannan[4], R. Saravanakumar[5], V. Subhashini[6], Dr.V. Jothi Francina[7], N. Deepa[8]

[1]Assistant Professor, Department of Mathematics, Government College of Engineering, Erode, Tamil Nadu, India. e-mail: asaigeethan14@gct.ac.in, orcid: https://orcid.org/0009-0001-0677-300X*
[2]Associate Professor, Department of Mathematics, Government College of Technology, Coimbatore, Tamil Nadu, India. e-mail: perumalsamy@gct.ac.in, orcid: https://orcid.org/0000-0002-5696-1615
[3]Assistant Professor, Department of Mathematics, Government College of Technology, Coimbatore, Tamil Nadu, India. e-mail: gnanakumar@gct.ac.in, orcid: https://orcid.org/0009-0000-3122-6967
[4]Assistant Professor, Department of Mathematics, Government College of Technology, Coimbatore, Tamil Nadu, India. e-mail: jduraikannan@gct.ac.in, orcid: https://orcid.org/0009-0009-2118-5490
[5]Lecturer, Department of Basic Science (Mathematics), PSG Polytechnic College, Coimbatore, Tamil Nadu, India. e-mail: saravanakumar12512@gmail.com, orcid: https://orcid.org/0009-0008-9437-579X
[6]Assistant Professor, Department of Mathematics, Erode Sengunthar Engineering College, Thudupathi, Tamil Nadu, India. e-mail: subhashini@esec.ac.in, orcid: https://orcid.org/0009-0005-3155-9725
[7]Assistant Professor, Department of Management Studies, Sona College of Technology, Salem, Tamil Nadu, India. e-mail: francyjothi@gmail.com, orcid: https://orcid.org/0000-0002-1705-6727
[8]Assistant Professor, Department of Mathematics, Government College of Technology, Coimbatore, Tamil Nadu, India. e-mail: dheepimath@gct.ac.in, orcid: https://orcid.org/0009-0006-3909-4923

Received: September 18, 2025; Revised: October 28, 2025; Accepted: December 01, 2025; Published: December 30, 2025

SUMMARY

This research investigates the Magnetohydrodynamic (MHD) flow of a Sutterby hybrid nanofluid over a convectively heated stretching sheet, specifically addressing the protection of human skin from solar thermal radiation. Utilizing Buongiorno's nanomaterial model, the study evaluates the synergy of Cadmium Selenide (CdSe) and $(C_6H_{11}NO_4)_n$ − Chitosan nanoparticles in mitigating radiation absorption. The governing nonlinear equations are transformed into ordinary differential equations and solved numerically. The analysis is conducted in two distinct phases. First, the physical flow dynamics are examined. Results indicate that an increase in the Deborah number (De) and Reynolds number (Re) enhances fluid velocity, while an intensified magnetic field (M) reduces flow speed due to the Lorentz

force. Thermal analysis reveals that the radiation parameter (Rd) and Eckert number (Ec) significantly thicken the thermal boundary layer, enhancing heat dissipation. Second, the study introduces a novel uncertainty analysis using Triangular Fuzzy Numbers (TFN) within the α range [0, 0.5, 1] to assess nanoparticle volume fractions. By employing the α-cut methodology and the Triangular Membership Function (TMF), the research evaluates the variability of the velocity and temperature profiles. Fuzzy linear regression demonstrates that the fuzzy velocity profile achieves its maximum flow rate at the central (crisp) value compared to the left and right membership bounds. These findings suggest that hybrid nanoparticles offer a superior internal defense mechanism against solar damage compared to topical treatments, providing a theoretical foundation for developing high-efficiency solar protection technologies.

Key Words: *sutterby hybrid nanofluid, solar radiation, homogeneous-heterogeneous, microorganism, triangular membership function, triangular fuzzy function.*

INTRODUCTION

Hayat et al., (2016) [1] examining how compliant walls affect the peristaltically induced flow of Sutterby fluid in a vertical medium, it was discovered that the fluid's temperatures and velocity distributions are larger than those of viscous fluid. Abdul Basit et al., (2023) [2] outlined the importance of parabolic surfaces for the movement of mass and heat through the flow of bio-convective Sutterby nanofluid and explained about the flow of the nanofluid over the parabolic surface. Sabir et al., (2021) [3] the effects of thermal radiation on Sutterby fluid that is travelling across an inclined surface were alleged to demonstrate. Usman et al., (2021) [4] studied the transmission of heat and mass on a curved stretching sheet as well as the non-Newtonian Sutterby nanofluid flow. Due to the presence of porosity and the curved stretched sheet, the Darcy-Forchheimer model is employed. The rulebook for motile microbes also includes gyrotactic microbes that swim by impact. Aldabesh et al., (2022) [5] Consider Sutterby nano-fluid involving microorganisms over stretched cylinder to see how parametric influences modify the character of challenges. Thermal radiation, Darcy resistance, and activation energy all play essential roles in demonstrating these effects. Extended issues at stationary points and stretched cylinders are explored using Fourier and Fick theories. Zeeshan et al., (2021) [6] explored nanofluids that maximize heat transmission and minimize energy loss. This fluid's heat transport depends on particle Brownian and thermophoresis motion. Heat transfer increases energy dissipation constraint and entropy generation decrease. Non-Newtonian Casson nano-fluid two-dimensional flow over a parabola's horizontal surface is explored. The chemical process parameter raised the temperature field, whereas the Casson fluid parameter lowered it. Haq et al., (2021) [7] examined mixed convection magnetohydrodynamic Casson nanomaterial flow using activation energy across a stretchy cylinder. The impacts of solutal, thermal, and motile density stratifications at the surface boundary are explored as well. Punith Gowda et al., (2021) [8] claimed that activation energy on non-Newtonian nanofluids is used for flow and heat transmission in a broad range of applications, such as coatings, oceanography, sus pensions, metallic plate coolants, heat exchangers, biological fluids of moving nature, and melt-spinning. Benhanifia et al., (2022) [9] examined the flow of Casson nanofluid through a cylindrical cylinder while mixing it, as well as the numerical findings that were generated using computational methods. Jamshed et al., (2022) [10] performed a simulation of the Williamson nanofluid, which consisted of nanoparticles of copper and aluminium oxide suspended in a base fluid of methanol and running through a semiconductor collector.

Cellular streaming patterns are found in liquid suspensions of swimming microorganisms. These patterns involve bulk fluid movements that occur downwards in areas where large concentrations of microorganisms develop and upwards in regions where low concentrations of microorganisms develop. Ali et al., (2020) [11] described how an examination of temperature changes with bioconvection of self-motivated microorganisms mixed in micropolar based nanofluids is carried out using an effective computational approach. The whole transit of concentration, momentum, and energy takes place around a point of stasis across a stretching/shrinking sheet. Khan et al., (2021) [12] Developed a contemporary mathematical framework to analyze the outcomes of magnetized viscous nano-fluid exhibiting bio-convection as it flows via diverse geometries (plate, wedge, and cone) under convective boundary conditions. Hayat et al., (2021) [13] Investigated the gyrotactic microorganisms were present during the investigation of the Prandtl-Eyring nanomaterial. Asjad et al., (2022) [14] studied on the motion of the nanofluids, which was a concept that was utilized efficiently to restrict the augmentation of heat

transmission that was induced by stretched sheets. Imran et al., (2022) [15] examined the physical properties of nanofluid flow influenced by bio-convection by parabolic rotation across a parallel surface using gyrotactic motile microorganisms. Freire et al., (2025) [16] investigates the effect of bio-convection on Williamson nanofluid flow, with a focus on the effectiveness of non-linear chemical reactions and heat radiation on stretching sheets. Awan et al., (2022) [17] explored the nano liquids with a magnetic field flowing across a porous needle that is rotating thin needles.

Thermal radiation is a kind of energy emitted by an energized body in all directions, travelling directly to the place of absorption. Ramesh et al., (2022) [18] Investigated the effects of suction on a two-dimensional, unstable natural convective flow of electrically conducting MHD nano-fluid across a linearly permeable stretched sheet, incorporating chemical reactions, Joule heating, viscous dissipation, and thermal radiation. Daniel et al., (2019) [19] endeavored to apply the Homotropy analysis approach to ascertain the governing constraints of heat transfer and fluid flow of a nanofluid across a flat surface. Venkata et al., (2019) [20], Dash et al., (2022) [21] examined thermal radiation in magnetohydrodynamic nanofluid across a moving vertical plate, resulting in the transfer of heat anomalies. Examined whether homogeneous and heterogeneous reactions in hybrid nanofluid systems depend on activation energy. For fluid-solid interface applications, this inclusion enhances thermofluidic-chemical process understand. Sadulla et al., (2023) [22] studied how modelling blood flow in constricted arteries, incorporating convective dynamics and wall features, affects homogeneous and heterogeneous reactions. Mondal et al., (2024) [23] explored magnetized Sisko fluid flow over an expanding sheet under convective boundary conditions using Buongiorno's homogeneous-heterogeneous response method. Haq et al., (2022) [26]; Vaidya et al., (2021) [24] studied how homogeneous and heterogeneous reactions and porous media affect hybrid nanofluid circulation across three surfaces. Both reaction types reduce flow dynamics, and a porous property reduces surface drag forces and improves thermal diffusion.

Fuzzy structure theory provides a valuable framework for comprehending phenomena in fluid dynamics, offering a more realistic approach than the assumption of crispness. The boundary conditions determining a fluid flow problem are indeterminate and may be regarded as variables characterised by fuzzy numbers. Ghasemi Moghaddam et al., (2020) [27]; Upreti et al., (2022) [25] considering the type of generalized Hukuhara differentiability, the work aimed to investigate fuzzy solutions for the fuzzy linear transport equation and the fuzzy wave equation. Ali et al., (2020) [11] developed the homotropy analysis method for addressing high-order ODE-based fuzzy initial value problems, encompassing both linear and nonlinear cases. Barhoi et al. (2018) [31] examined the imprecise representation of certain variables and parameters in fluid mechanics equations. Subsequently, they employed the Zadeh extend technique to ascertain the fuzzy implications. Biswal et al., (2020) [32]; Moatimid et al., (2024) [28] explored the natural convection of a nanofluid flow in an unpredictable environment using high-performance magnetism (HPM) over two plates of comparable size. Obtaining both the volume fraction of nanoparticles and TFN (an acronym for both) was determined. Dubois et al., (1978) [33]; Geetha et al., (2025) [29] set up mathematical procedures for three varieties of fuzzy numbers: triangle, trapezium, and Gaussian. For the sake of thoroughness, TFNs are listed. Seikkala et al., (1987) [35]; Jameel et al., (2014) [30]; Deepika et al., (2026) [34] familiar with the notion of fuzzy derivatives.

In this research paper, it has been examined the radiative magnetohydrodynamic (MHD) flow of a Sutterby hybrid nanofluid beyond a stretching sheet and take into account both homogeneous and heterogeneous reactions in this work. The main goal is to reduce the adverse effects that sun thermal radiation does to human skin. By putting nanoparticles into the body, it hopes to lower the amount of radiation that gets into the bloodstream through the skin. This could be a better way to help people who are out in the sun for a long time than using regular sunscreens, lotions, or sprays. The properties of the nanomaterial are put together using Buongiorno's nanomaterial model. Here explored are the two sections. The first is heating transfer analysis, which is carried out in the presence of thermal radiation. Joule heating and viscous dissipation effects and the combined effects of Brownian motion and thermophoresis due to the presence of nanoparticles are considered. The second is Fuzzy differential equations (FDEs) are employed to calculate the volumetric ratio of nanoparticles linked to quantity uncertainty distribution. Consequently, the volume proportions of the hybrid nanofluid are regarded as TFNs (triangular fuzzy numbers), and the α-cut method is employed to ascertain the volume fractions.

The imprecise TMF (triangular membership function) elucidates the α-cut.

The existing literature highlights the significant thermal and velocity advantages of Sutterby fluids over traditional viscous fluids. Previous studies have explored these dynamics across various geometries, such as parabolic surfaces and curved stretching sheets, often employing the Darcy-Forchheimer model to account for porosity. Research into bioconvection has established that gyrotactic microorganisms significantly influence flow challenges and thermal management. Furthermore, studies on fuzzy structure theory argue that assuming "crisp" values in fluid dynamics is often unrealistic, suggesting that fuzzy differential equations provide a more precise framework for handling boundary condition uncertainties.

This research builds upon these findings by integrating Sutterby hybrid nanofluids (using CdSe and Chitosan) with fuzzy logic (Triangular Fuzzy Numbers) to address the specific real-world challenge of protecting human skin from solar thermal radiation. While prior literature focused on general heat transfer, this study uniquely applies these complex dynamics to enhance internal defense mechanisms against prolonged sun exposure.

To enhance the introduction of your study, here are the requested sections based on the analysis of your research:

Key Contributions

- Investigates the synergistic effects of Cadmium Selenide (CdSe) and Chitosan nanoparticles in a Sutterby fluid to optimize solar radiation protection.
- Incorporates Triangular Fuzzy Numbers (TFN) and α-cut methodology to analyze the impact of imprecise nanoparticle volume fractions on flow dynamics.
- Integrates gyrotactic microorganisms and chemical reactions into the MHD Sutterby model to analyze their influence on thermal and mass transport.

The manuscript, the paper is organized into the following eight sections: The study begins with an Introduction (Section 1) reviewing literature. Fuzzy Concept (Section 2) defines mathematical fuzzy sets, followed by Mathematical Formulation (Section 3) of the flow equations. Methodology (Section 4) details the numerical bvp5c solution. Physical Estimations (Section 5) defines engineering parameters, while Formulation of Fuzzification (Section 6) integrates uncertainty. Finally, Results and Discussion (Section 7) analyze graphical data, concluding with Conclusion (Section 8).

FUZZY CONCEPT

Definition 1. A fuzzy set $\tilde{A} \subseteq X$ is a set to describe the fuzzy concept, which are not crisp and be defined as a set of ordered pairs and it can be represented mathematically as

$\tilde{A} = \{(\eta, \mu_{\tilde{A}}(\eta)): f \in U, \mu_{\tilde{A}}(\eta) \in [0,1]\}$. where $\mu_{\tilde{A}}(f)$ are a membership function of $\tilde{A}$, X – universal set, the mapping is measured as $\mu_{\tilde{A}}(\eta): U \longrightarrow [0,1]$.

Definition 2. An $\alpha - cut$ of a fuzzy set $\tilde{A}$ is a crisp set $A_\alpha \subseteq X$ such that $A_\alpha = \{\eta/\mu_{\tilde{A}}(\eta) \geq \alpha\}$, $\alpha \in [0,1]$.

Definition 3. Let triangular fuzzy number (TFN) $\tilde{A} = (\epsilon_1, \epsilon_2, \epsilon_3)$ along with membership function $\mu_{\tilde{A}}(\eta)$ explicate as in equation (1),

$$\mu_{\tilde{A}}(\eta) = \begin{cases} \frac{\eta - \epsilon_1}{\epsilon_2 - \epsilon_1}, \text{for } \epsilon_1 \leq \eta \leq \epsilon_2 \\ \frac{\epsilon_3 - \eta}{\epsilon_3 - \epsilon_2}, \text{for } \epsilon_2 \leq \eta \leq \epsilon_3 \\ 0, \quad \text{elsewhere} \end{cases} \tag{1}$$

A TFN having a maximum (or center)ϵ_2, right width $\epsilon_3 - \epsilon_2 > 0$, and left width $\epsilon_2 - \epsilon_1 > 0$, is converted into interval numbers with the α-cut methodology and articulated as $\tilde{A} = \{[f'''_1(\eta,\alpha), f_2'(\eta,\alpha)]; [\theta_1(\eta,\alpha), \theta_2(\eta,\alpha)]; [m_1(\eta,\alpha), m_2(\eta,\alpha)]\} = [\epsilon_1+(\epsilon_2 - \epsilon_1)\alpha, \quad \epsilon_3 -(\epsilon_3 - \epsilon_2)\alpha]$, where $\alpha \in [0,1]$. An essential part of fuzzy set theory, the membership function is defined by it. Figure. 1 illustrates TFNs $\tilde{A} =(\epsilon_1, \epsilon_2, \epsilon_3)$ and the α-cut membership function. An arbitrary TFN saturates the ensuing conditions:

1. $f'_1(\eta,\alpha), \theta_1(\eta,\alpha), m_1(\eta,\alpha)$ and $\chi_1(\eta,\alpha)$ are functions that increase on the interval [0, 1].
2. $f'_2(\eta,\alpha), \theta_2(\eta,\alpha), m_2(\eta,\alpha)$ and $\chi_2(\eta,\alpha)$ are functions that decrease on the interval [0, 1].
3. $f'_1(\eta,\alpha) \leq f'_2(\eta,\alpha)$, $\theta_1(\eta,\alpha) \leq \theta_2(\eta,\alpha)$, $m_1(\eta,\alpha) \leq m_2(\eta,\alpha)$ and $\chi_1(\eta,\alpha) \leq \chi_2(\eta,\alpha)$ on the interval [0, 1].

$f'_1(\eta,\alpha), f'_2(\eta,\alpha), \theta_1(\eta,\alpha), \theta_2(\eta,\alpha), m_1(\eta,\alpha), m_2(\eta,\alpha), \chi_1(\eta,\alpha)$and $\chi_2(\eta,\alpha)$ are limited at [0, 1].

- $f'_1(\eta,\alpha) = f'_2(\eta,\alpha) = f'(\eta)$, [$f'(\eta)$ is a crisp velocity].
- $\theta_1(\eta,\alpha) = \theta_2(\eta,\alpha) = \theta(\eta)$, [$\theta(\eta)$ is a crisp temperature].
- $m_1(\eta,\alpha) = m_2(\eta,\alpha) = m(\eta)$, [$m(\eta)$ is a crisp concentration].
- $\chi_1(\eta,\alpha) = \chi_2(\eta,\alpha) = \chi(\eta)$, [$\chi(\eta)$ is a crisp microorganism].

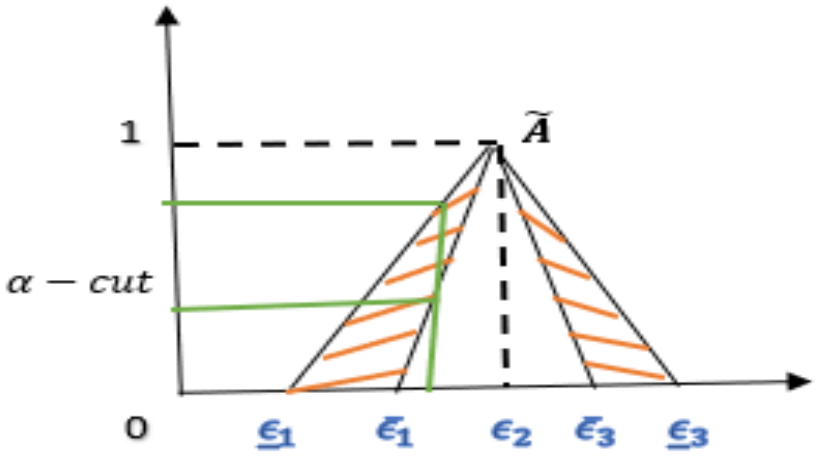

Figure 1. The membership functions of a TFN

MATHEMATICAL FORMULATION

Consider the two-dimensional incompressible boundary layer flow of nanofluid over a convectively heated stretching sheet located at $y = 0$. The sheet is stretched through two equal and opposite forces along x-axis by keeping the origin fixed with the velocity $U_w = ax$. Let $U_1(x) = bx$ be the fluid's velocity outside the boundary layer. A uniform magnetic field of strength B_0 is applied perpendicular to the direction to the flow. The induced magnetic field is neglected upon the assumption of small magnetic Reynolds number. Further, it is also assumed that the external electrical field is zero and the electric field due to the polarization of charges is negligible. The steady boundary layer equations governing the two-dimensional incompressible stagnation-point flow of nano fluid and utilizing the previously delineated assumptions, the simplified homogeneous-heterogeneous reactions can be articulated as follows in equation (2):

$$\mathbb{A} + 2\mathbb{B} \rightarrow 3\mathrm{B}, \qquad \text{rate} = d_c \alpha \beta^2, \tag{2}$$

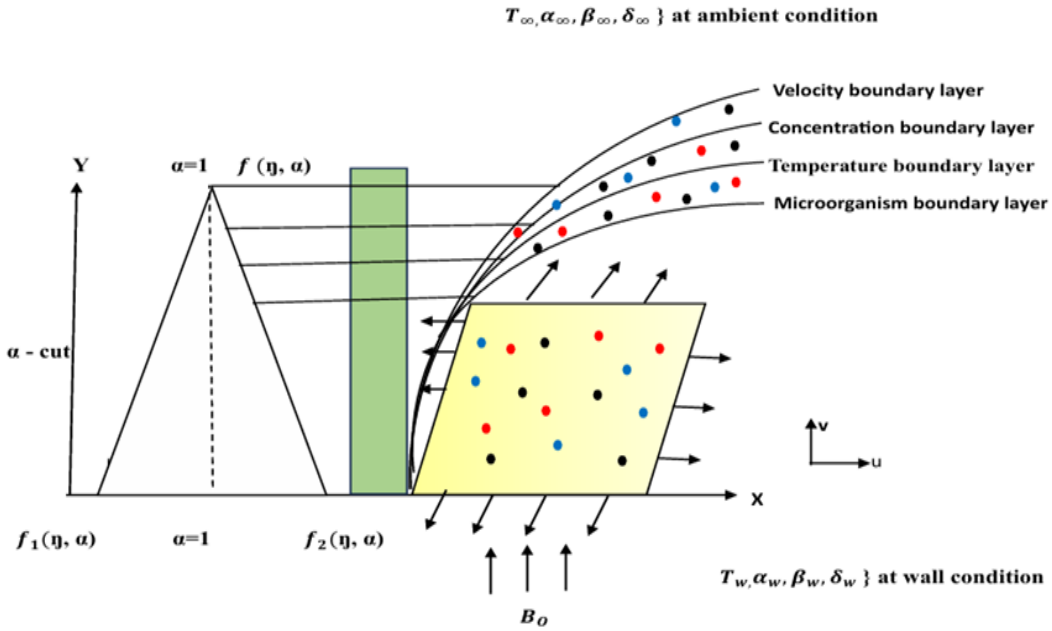

Figure 2. Thermal flow physical model

Figure 2 presents the physical configuration of the MHD Sutterby hybrid nanofluid flow over a convectively heated stretching sheet. It illustrates the coordinate system where the magnetic field and thermal radiation interact with the fluid containing CdSe-Chitosan nanoparticles and gyrotactic microorganisms, highlighting the boundary layer mechanisms for solar protection.

A single isothermal reaction of the first order is being carried out at the surface of the catalyst shown in equation (3) (4) follows,

$$\mathbb{A} \to \mathbb{B}, \text{ rate} = d_s \alpha, \tag{3}$$

$$\mathrm{u}\frac{\partial \mathrm{u}}{\partial \mathrm{x}} + \mathrm{v}\frac{\partial \mathrm{u}}{\partial \mathrm{y}} = 0, \tag{4}$$

$$\mathrm{u}\frac{\partial \mathrm{u}}{\partial \mathrm{x}} + \mathrm{v}\frac{\partial \mathrm{u}}{\partial \mathrm{y}} = \frac{\mu_{\mathrm{hnf}}}{\rho_{\mathrm{hnf}}}\left[\frac{\partial^2 \mathrm{u}}{\partial \mathrm{y}^2} + \frac{\mathrm{nE}^2}{2}\left(\frac{\partial \mathrm{u}}{\partial \mathrm{y}}\right)^2 \frac{\partial^2 \mathrm{u}}{\partial \mathrm{y}^2}\right] - \frac{\sigma \mathrm{B}_0^2}{\rho_{\mathrm{hnf}}}(\mathrm{u} - \mathrm{u}_\infty), \tag{5}$$

$$\mathrm{u}\frac{\partial \mathrm{T}}{\partial \mathrm{x}} + \mathrm{v}\frac{\partial \mathrm{T}}{\partial \mathrm{y}} = \alpha\,\frac{\partial^2 \mathrm{T}}{\partial \mathrm{y}^2} + \frac{\nu_{\mathrm{hnf}}}{\mathrm{C}_{\mathrm{hnf}}}\left(\frac{\partial \mathrm{u}}{\partial \mathrm{y}}\right)^2 - \frac{1}{(\rho \mathrm{c})_{\mathrm{hnf}}}\left(\frac{\partial \mathrm{q_r}}{\partial \mathrm{y}}\right) + \frac{\sigma_{\mathrm{hnf}} \mathrm{B}_0^2}{(\rho \mathrm{c})_{\mathrm{f}}}(\mathrm{u}_\infty - \mathrm{u})^2 + \tau\left[\mathrm{D_B}\frac{\partial \beta}{\partial \mathrm{y}}\frac{\partial \mathrm{T}}{\partial \mathrm{r}} + \frac{\mathrm{D_T}}{\mathrm{T}_\infty}\left(\frac{\partial \mathrm{T}}{\partial \mathrm{y}}\right)^2\right], \tag{6}$$

$$\mathrm{u}\frac{\partial \alpha}{\partial \mathrm{x}} + \mathrm{v}\frac{\partial \alpha}{\partial \mathrm{y}} = \mathrm{D}_\alpha \frac{\partial^2 \alpha}{\partial \mathrm{y}^2} + \frac{\mathrm{D_T}}{\mathrm{T}_\infty}\frac{\partial^2 \mathrm{T}}{\partial \mathrm{y}^2} - d_c \alpha \beta^2, \tag{7}$$

$$\mathrm{u}\frac{\partial \beta}{\partial \mathrm{x}} + \mathrm{v}\frac{\partial \beta}{\partial \mathrm{y}} = \mathrm{D}_{\boldsymbol{\beta}} \frac{\partial^2 \beta}{\partial \mathrm{y}^2} + \frac{\mathrm{D_T}}{\mathrm{T}_\infty}\frac{\partial^2 \mathrm{T}}{\partial \mathrm{y}^2} + d_s \alpha \beta^2, \tag{8}$$

$$\mathrm{u}\frac{\partial \mathrm{M}}{\partial \mathrm{x}} + \mathrm{v}\frac{\partial \mathrm{M}}{\partial \mathrm{y}} = \mathrm{D_M}\left(\frac{\partial^2 \mathrm{M}}{\partial \mathrm{y}^2}\right) - \frac{\mathrm{b^* W_c}}{(\mathrm{C_W} - \mathrm{C}_\infty)}\left[\frac{\partial}{\partial \mathrm{y}}\left(\mathrm{M}\frac{\partial \beta}{\partial \mathrm{y}}\right)\right]. \tag{9}$$

$$u = U_w(x) = lx + b_1\frac{\partial u}{\partial y}, v = 0, T = T_w + b_2\frac{\partial T}{\partial y}, \mathrm{D_A}\left(\alpha_w + b_3\frac{\partial \alpha}{\partial y}\right) = l_s\alpha, \mathrm{D_B}\left(\beta_w + b_3\frac{\partial \beta}{\partial y}\right) = -l_s\beta, M = M_w + b_4\frac{\partial M}{\partial y} \text{ at } y \to 0, u = U_\infty(x) = px, T \to T_\infty, a \to a_\infty, b \to b_\infty \text{ at } y \to \infty. \tag{10}$$

A and B are the concentrations of hybrid nano particles, $U_w(x) = lx$ is a liner velocity, where $l > 0$ is the parameter of constant acceleration, x is an independent variable, l_s is the characteristic length, m and n are nanoparticle concentrations$[mol/m^3]$, D_A and D_B are the Brownian diffusion

coefficients$[m^2/s]$, D_T is the thermophoresis diffusion coefficient$[m^2/s]$, u and v are velocity components $[m/s]$, $(C_p)_{hnf}$ is the specific heat of thnf $[J/kg.K]$, μ_{hnf} is the dynamic viscosity of the thnf $[kgm^{-1}s^{-1}]$, $\rho_{hnf}$is the density of thnf $[kg/m^3]$, $(\rho C_p)_{hnf}$ is the heat capacitance of thnf $[J/kg.K]$, ν_{hnf} is the kinematic viscosity of the thnf $[m^2/s]$, k_{hnf} is the thermal conductivity of thnf $[W/m.K]$, α_{hnf} is the thermal diffusivity of the thnf $[m^2/s]$, n is the power law index number, and the effective fluid heat capacity $\alpha = \frac{(\rho C)_f}{(\rho C)_p}$ and q_r is the radiative heat flux. Using the Rosseland approximation for thermal radiation and applying to optically thick media, the radiative heat flux is given by [32] in equation (11),

$$q_r = -\frac{4\sigma^*}{3k^*}\frac{\partial T^4}{\partial y} = -\frac{16\sigma^*}{3k^*}\,T^3\frac{\partial T}{\partial y}, \tag{11}$$

Where σ^* and k^* are the Stefan-Boltzmann constant and the mean absorption coefficient.

Introducing the following transformation to convert governing equations into dimensionless form represents in equation (12)

$$\eta = \sqrt{\frac{a}{\upsilon_f}}y,\ u = axf'(\eta), v = -\sqrt{a\upsilon_f}f(\eta),\ \ \theta(\eta) = \frac{T-T_\infty}{T_f-T_\infty} \text{ with } T = T_\infty(1+(\theta_w-1)\theta), M(\eta) = \frac{M-M_\infty}{M_w-M_\infty} \text{ and } m(\eta) = \frac{\alpha-\alpha_\infty}{\alpha_w-\alpha_\infty}, n(\eta) = \frac{\beta-\beta_\infty}{\beta_w-\beta_\infty}. \tag{12}$$

The righthand side of the eqns. (5) and (10) given,

$$\mathrm{u}\frac{\partial \mathrm{T}}{\partial \mathrm{x}} + \mathrm{v}\frac{\partial \mathrm{T}}{\partial \mathrm{y}} = \frac{\partial}{\partial \mathrm{y}}\left[\left(\alpha + \frac{16\sigma^* T^3}{3(\rho \mathrm{c})_{\mathrm{hnf}}\,k^*}\right)\frac{\partial \mathrm{T}}{\partial \mathrm{y}}\right]\frac{\partial^2 \mathrm{T}}{\partial \mathrm{y}^2} + \frac{\nu_{\mathrm{hnf}}}{\mathrm{C}_{\mathrm{hnf}}}\left(\frac{\partial \mathrm{u}}{\partial \mathrm{y}}\right)^2 - \frac{1}{(\rho \mathrm{c})_{\mathrm{hnf}}}\left(\frac{\partial \mathrm{q_r}}{\partial \mathrm{y}}\right) + \frac{\sigma_{\mathrm{hnf}}\mathrm{B}_0^2}{(\rho \mathrm{c})_{\mathrm{hnf}}}(\mathrm{u}_\infty - \mathrm{u})^2 + \tau\left[\mathrm{D_B}\left(\frac{\partial \mathrm{A}}{\partial \mathrm{y}} + \frac{\partial \mathrm{B}}{\partial \mathrm{y}}\right)\frac{\partial \mathrm{T}}{\partial \mathrm{y}} + \frac{\mathrm{D_T}}{\mathrm{T}_\infty}\left(\frac{\partial \mathrm{T}}{\partial \mathrm{y}}\right)^2\right], \tag{13}$$

The first term on the righthand side of eqn. (12) can be written as

$\alpha\frac{\partial}{\partial \mathrm{y}}\left[\frac{\partial \mathrm{T}}{\partial \mathrm{y}}(1 + R_d(1+(\theta_w-1)\theta^3)\right]$, where R_d is the radiation parameter and it is denoted by $\frac{16\sigma^* T_\infty^3}{3kk^*}$, if $R_d = 0$ gives no thermal radiation effect.

After applying the described transformation, the governing equations (5), (6), (7), (8), (9), (10) and (13) takes the following form

$$\frac{f'''(\eta)}{A_1A_2}\left[1 + \frac{n}{2}D_e Re_x (f''(\eta))^2\right] - (f'(\eta))^2 + f(\eta)\,f''(\eta) + \frac{A_4A_5}{A_2}B\big(\lambda - f'(\eta)\big) = 0, \tag{14}$$

$$\frac{1}{Pr}[(1 + R_d(1+(\theta_w-1)\theta^3)\,\theta'(\eta)]' + f\theta' + \frac{1}{A_1A_2}Ecf''^2 + \frac{A_4A_5}{A_3}BEc(\lambda - f'(\eta))^2 + Nb\chi'\theta' + Nt(\theta')^2 = 0, \tag{15}$$

$$\frac{1}{Sc}\left[m''(\eta) + \frac{N_t}{N_b}\theta''(\eta)\right] + f(\eta)\,m'(\eta) - Lmn^2 = 0, \tag{16}$$

$$\frac{\delta}{Sc}\left[n''(\eta) + \frac{N_t}{N_b}\theta''(\eta)\right] + f(\eta)\,n'(\eta) + Lmn^2 = 0, \tag{17}$$

$$\chi''(\eta) - Pe[m''(\eta)(\chi(\eta)+\omega) + m'(\eta)\chi'(\eta)] + Lbf(\eta)\,\chi'(\eta) = 0. \tag{18}$$

Associated boundary conditions

$$f(0) = 0,\ f'(0) = 1 + b_1 f''(0), \theta(0) = 1 + b_2\theta'(0),\ L_s m'(0) = 1 + b_3 m(0),\ \delta L_s n'(0) = -(1 + b_3 n(0)),\ \chi(0) = 1 + b_4\chi'(0), f'(\infty) = \lambda, \theta(\infty) = 0, m(\infty) = 1, n(\infty) = 1, \chi(\infty) = 0. \tag{19}$$

Assume that the diffusion coefficient D_A and D_B are equal $i.e., \alpha = 1$, then

$$m(\eta) + n(\eta) = 1, \tag{20}$$

The concentration equations (14), (15), (16), (17) converts to the form by above transformation

$$\frac{1}{Sc}\left[m''(\eta) + \frac{N_t}{N_b}\theta''(\eta)\right] + f(\eta)\, m'(\eta) - Lm(1-m)^2 = 0, \tag{21}$$

Subject to the boundary condition

$$m'(0) = L_s m(0),\ m(\infty) = 1 \tag{22}$$

Table 1. Nomenclatures and default values for physical parameters

Curvature Parameter	$\boldsymbol{D_e}$	$\frac{E^2a^2}{v_f}$
Material Parameter	$\boldsymbol{Re_x}$	$\frac{a^2x}{v_f}$
Magnetic Field Parameter	$\boldsymbol{B}$	$\frac{\sigma_f B_0^2}{\rho_f a}$
Velocity ratio	$\boldsymbol{\lambda}$	$\frac{p}{l}$
Prandtl number	$\boldsymbol{Pr}$	$\frac{v_f}{\alpha}$
Eckert number	$\boldsymbol{Ec}$	$\frac{U_w^2}{C_f}$
Schmidt number	$\boldsymbol{Sc}$	$\frac{v_f}{D_A}$
Ratio Diffusion coefficients	$\boldsymbol{\delta}$	$\frac{D_B}{D_A}$
Brownian motion	$\boldsymbol{N_b}$	$\frac{\tau D_B(e_w - e_\infty)}{\sigma_f}$
Thermophoresis limiting factor	$\boldsymbol{N_t}$	$\frac{\tau D_T(T_w - T_\infty)}{T_\infty \sigma_f}$
Peclet number	$\boldsymbol{Pe}$	$\frac{b^* W_c}{D_m}$
Lewis number	$\boldsymbol{Lb}$	$\frac{v_f}{D_m}$
Microorganism difference parameter	$\boldsymbol{\omega}$	$\frac{M_\infty}{M_w - M_\infty}$

Notation	Hybrid nanofluid approximation
A	$[(1-\varphi_1)^{2.5}(1-\varphi_2)^{2.5}]$
$\boldsymbol{A_2}$	$(1-\varphi_2)\left[(1-\varphi_1)+\varphi_1\frac{\rho_{s1}}{\rho_f}\right]+\varphi_2\frac{\rho_{s2}}{\rho_f}$
$\boldsymbol{A_3}$	$\left[\left((1-\varphi_2)\left[(1-\varphi_1)+\varphi_1\frac{(\rho c)_{s1}}{(\rho c)_f}\right]+\varphi_2\frac{(\rho c)_{s2}}{(\rho c)_f}\right)\right]$
$\boldsymbol{A_4}$	$\left(\frac{\sigma_2+2\sigma_{nf}-2\varphi_2(\sigma_{nf}-\sigma_2)}{\sigma_2+2\sigma_{nf}+\varphi_2(\sigma_{nf}-\sigma_2)}\right)$
$\boldsymbol{A_5}$	$\left(\frac{\sigma_1+2\sigma_f-2\varphi_1(\sigma_f-\sigma_1)}{\sigma_1+2\sigma_f+\varphi_1(\sigma_f-\sigma_1)}\right)$

Table 1 systematically presents the thermophysical parameters and nondimensional constants, such as the Prandtl number, Eckert number, and Peclet number, utilized in the numerical simulation. The table links each physical property to its mathematical notation and provides the specific hybrid nanofluid approximation values necessary for evaluating the flow dynamics. This comprehensive dataset ensures the reproducibility of the study and establishes the baseline environment for analyzing the Sutterby fluid's behavior under magnetic and radiative influences.

METHODOLOGY

The system of First-order ordinary differential equations (14), (15), (18) and (21) with boundary conditions (19), (20), (22), (23), (24), (25) are numerically carried out through the bvp5c in MATLAB. This technique is a very efficient mathematical tool for tackling the highly nonlinear problems. The residual of the continuous solution is applied for lattice selection and error control. Accordingly, the previously mentioned ODEs are transformed into a first-order system, with Equations (14), (15), (18) and (21) taking the following forms:

$$f=g_1, f'=g_2, f''=g_3, f'''=g_3', \theta=g_4, \theta'=g_5, \theta''=g_5', m=g_6, m'=g_7, m''=g_7', \chi=g_8, \chi'=g_9, \chi''=g_9', \tag{23}$$

$$G_1=g_3'=f'''=\frac{A_1A_2\left[f'^2-ff''-\frac{A_4A_5}{A_2}B\left(\lambda-f'(\eta)\right)\right]}{1+\frac{n}{2}D_eRe_x(f'')^2}, \tag{24}$$

$$G_2=g_5'=\frac{-\left[f\theta'+\frac{1}{D_3D_4}Ecf''^2+\frac{D_1D_2}{D_5}BEc(\lambda-f')^2+Nb(m'+n')\theta'+Nt(\theta')^2\right]}{\frac{1}{Pr}(1+R_d(1+(\theta_w-1)\theta^3)}, \tag{25}$$

$$G_3=g_7'=\frac{-\left[m'(\eta)f(\eta)+\frac{1}{ScN_b}N_t\theta''(\eta)\right]+Lm(1-m)^2}{\frac{1}{Sc}}, \tag{26}$$

$$G_4=g_9'=Pe[\chi(\eta).m''(\eta)-m'(\eta)\chi'(\eta)]-Lbf(\eta)\,\chi'(\eta) \tag{27}$$

With boundary conditions:

$$f(0)=0,\ f'(0)=1+b_1f''(0), \theta(0)=1+b_2\theta'(0),\ L_sm'(0)=1+b_3m(0),\ \chi(0)=1+b_4\chi'(0), f'(\infty)=\lambda, \theta(\infty)=0, m(\infty)=1, \chi(\infty)=0. \tag{28}$$

Prior to using the boundary value problem method (bvp5c) to solve a set of first-order ordinary differential equations (ODEs chose detrimental initial estimates for $g_3(0), g_5(0), g_7(0)$ and $g_9(0)$ as -1, 1, 1, and 1, respectively shown in equation (26), (27), (28),. So, until the required convergence conditions are met, if the accepted error is less than the border residuals of G_1, G_2, G_3 and G_4, then the process will continue.

PHYSICAL ESTIMATIONS

$$Cf_x = \frac{2\tau_w}{\rho u_w^2}, Nu_x = \frac{xq_w}{k(T_f - T_\infty)}, Sh_x = \frac{xm_w}{D_B(C_w - C_\infty)}, Nh_x = \frac{xn_w}{D_m(N_w - N_\infty)}, \quad (29)$$

Shear stress, heat, mass and motile density microorganism are given by

$$\tau_w = -\mu_0 \left[\frac{\partial u}{\partial y} + \frac{mE^2}{6}\left(\frac{\partial u}{\partial y}\right)^3\right]_{y=0}, q_w = -k\left(\frac{\partial T}{\partial y}\right), m_w = -k\left(\frac{\partial C}{\partial y}\right), n_w = -k\left(\frac{\partial N}{\partial y}\right). \quad (30)$$

The dimensionless form of the above parameters is expressed as

$$\sqrt{Re_x} Cf_x = \left[f''(0) + \frac{1}{6} mDe_S\, Re_x \left(f''(0)\right)^3\right], \quad (31)$$

$$\frac{1}{\sqrt{Re_x}}\, Nu_x = -\left(1 + \frac{4}{3}Rd\right)\theta'(0), \quad (32)$$

$$\frac{1}{\sqrt{Re_x}} Sh_x = -\phi'(0), \quad (33)$$

$$\frac{1}{\sqrt{Re_x}} Nh_x = -\chi'(0). \quad (34)$$

where $Re_x = \frac{ax^2}{\upsilon_f}$ is the local Reynolds number.

The physical quantities of engineering interest, including skin friction coefficient, local Nusselt number, Sherwood number, and motile density rate, are defined in Equation (29). These represent the surface shear stress and the transport rates of heat, mass, and microorganisms, respectively. The fundamental surface gradients for momentum and energy are detailed in Equation (30), incorporating the Sutterby fluid parameters. Through the boundary layer transformation, these quantities are reduced to the dimensionless expressions found in Equation (31) computes the skin friction using the local Reynolds number (Rex), while Equations (32) (33) through (34) describe the heat transfer rate involving the radiation parameter (Rd), mass transfer, and microorganism density gradients at the surface (y=0).

FORMULATION OF FUZZIFICATION

Additionally, this research looks into comparing tri-nanofluids using fuzzy notions. Obtaining the volume proportion of the thnf as a TFN follows the transformation of the non-linear ODEs into FDS. MATLAB initiative bvp5c was used. An immediate shift in the volume-to-flow ratio of thnf influences the flow's heat and pace. These factors are the only ones that can determine the heat transmission and flow rate of the thnf. According to some researchers, the volume of nanoparticles is between [0.01-0.04]. Since φ_1 and φ_2 represent the volume proportion of nanoparticles $CdSe$, and $(C_6H_{11}NO_4)_n$ in a fuzzy context, it is possible to approach a difficult case by obtaining the volume fractions as a TFN. Table 2 defines the properties of the nanoparticle. The TFNs, which are the volume fractions of thnf used in this study, are transformed into α-cut procedures, which control the fuzziness of the TFNs.

Table 2 displays the fuzzy numbers in triangle form together with their crisp values. The significance of the fuzzy number at each α-cut was determined by utilizing TFNs that ranged from 0 to 1. For fuzzy numbers, the TFNs specify the triangle membership functions. Nonlinear ODEs (14), (15), (18) and (21) were converted into FDEs with their respective boundary conditions for fuzzy solutions by utilizing a fuzzy process and the α-cut approach.

$$\frac{1}{A_1A_2}\frac{d^3}{d\eta^3}[f_1(\eta,\alpha), f_2(\eta,\alpha)]\left[1 + \frac{n}{2}D_e Re_x\left(\frac{d^2}{d\eta^2}[f_1(\eta,\alpha), f_2(\eta,\alpha)]\right)^2\right] - \left(\frac{d}{d\eta}[f_1(\eta,\alpha), f_2(\eta,\alpha)]\right)^2 +$$
$$[f_1(\eta,\alpha), f_2(\eta,\alpha)].\frac{d^2}{d\eta^2}[f_1(\eta,\alpha), f_2(\eta,\alpha)] + \frac{A_4A_5}{A_2} B\left(\lambda - \frac{d}{d\eta}[f_1(\eta,\alpha), f_2(\eta,\alpha)]\right) = 0, \quad (35)$$

$$\frac{1}{Pr}\left[(1+R_d(1+(\theta_w-1)\theta^3)\ \frac{d}{d\eta}[\theta_1(\eta,\alpha),\theta_2(\eta,\alpha)]\right]'+[f_1(\eta,\alpha),f_2(\eta,\alpha)].\frac{d}{d\eta}[\theta_1(\eta,\alpha),\theta_2(\eta,\alpha)]+$$
$$\frac{1}{A_1A_2}Ec\left(\frac{d^2}{d\eta^2}[f_1(\eta,\alpha),f_2(\eta,\alpha)]\right)^2+\frac{A_4A_5}{A_3}BEc\left(\lambda-\frac{d}{d\eta}[f_1(\eta,\alpha),f_2(\eta,\alpha)]\right)^2+$$
$$Nb\frac{d}{d\eta}[\chi_1(\eta,\alpha),\chi_2(\eta,\alpha)].\frac{d}{d\eta}[\theta_1(\eta,\alpha),\theta_2(\eta,\alpha)]+Nt\left(\frac{d}{d\eta}[\theta_1(\eta,\alpha),\theta_2(\eta,\alpha)]\right)^2=0, \quad (36)$$

$$\frac{1}{Sc}\left[\frac{d^2}{d\eta^2}[m_1(\eta,\alpha),m_2(\eta,\alpha)]+\frac{N_t}{N_b}\frac{d^2}{d\eta^2}[\theta_1(\eta,\alpha),\theta_2(\eta,\alpha)]\right]+$$
$$[f_1(\eta,\alpha),f_2(\eta,\alpha)]\frac{d}{d\eta}[m_1(\eta,\alpha),m_2(\eta,\alpha)]-L[m_1(\eta,\alpha),m_2(\eta,\alpha)](1-[m_1(\eta,\alpha),m_2(\eta,\alpha)])^2=0 \quad (37)$$

$$\frac{d^2}{d\eta^2}[\chi_1(\eta,\alpha),\chi_2(\eta,\alpha)]-Pe\left[[\chi_1(\eta,\alpha),\chi_2(\eta,\alpha)].\frac{d^2}{d\eta^2}[m_1(\eta,\alpha),m_2(\eta,\alpha)]+\right.$$
$$\left.\frac{d}{d\eta}[\chi_1(\eta,\alpha),\chi_2(\eta,\alpha)].\frac{d}{d\eta}[m_1(\eta,\alpha),m_2(\eta,\alpha)]\right]+Lb[f_1(\eta,\alpha),f_2(\eta,\alpha)]\ \frac{d}{d\eta}[\chi_1(\eta,\alpha),\chi_2(\eta,\alpha)]=0, \quad (38)$$

The consistent boundary conditions are.

$$[f_1(0,\alpha),f_2(0,\alpha)]=0,\frac{d}{d\eta}[f_1(0,\alpha),f_2(0,\alpha)]=1+b_1\frac{d^2}{d\eta^2}[f_1(0,\alpha),f_2(0,\alpha)],[\theta_1(0,\alpha),\theta_2(0,\alpha)]=$$
$$1+b_2\frac{d}{d\eta}[\theta_1(0,\alpha),\theta_2(0,\alpha)],\ L_s\frac{d}{d\eta}[m_1(0,\alpha),m_2(0,\alpha)]=1+$$
$$b_3[m_1(\eta,\alpha),m_2(\eta,\alpha)],[m_1(\infty,\alpha),m_2(\infty,\alpha)]=1\ ,[\chi_1(0,\alpha),\chi_2(0,\alpha)]=1+$$
$$b_4\frac{d}{d\eta}[\chi_1(0,\alpha),\chi_2(0,\alpha)],\frac{d}{d\eta}[f_1(\infty,\alpha),f_2(\infty,\alpha)]=\lambda,[\theta_1(\infty,\alpha),\theta_2(\infty,\alpha)]=0. \quad (39)$$

Equations are the fuzzy form of the governing dimensionless equations that include uncertainty in the form of alpha-cut methodology and Triangular Fuzzy Numbers (TFN). Particularly, Equation (35) characterizes the fuzzy energy balance, which takes into consideration thermal radiations, the Joule heating and viscous dissipation under the condition of inaccurate nanoparticle volume fractions. The fuzzy concentration profile is modeled in equation (36), which combines both the effects of the Brownian motion and thermophoresis in presence of uncertainty. The fuzzy bioconvection equation of microorganisms is elaborated in Equation (37) that shows the interaction of the motile density and the concentration gradient. Lastly, Equation (38) defines the regular values of fuzzy boundary conditions at the stretching sheet and ambient state, such that the physical system is stable to any membership values within the range of α [0, 1].

Table 2. TFNs of fuzzy hybrid nanoparticles of volume proportion

Crisp Value for nano particles		**TFN**	**$\alpha-$ cut approach**
$\varphi_1(\boldsymbol{CdSe})$	0.03	$[0, 0.5, 1]$	$[0.5\alpha, 1-0.5\alpha], \alpha \in [0\ ,1]$
$\varphi_2(\boldsymbol{C_6H_{11}NO_4})_n$	0.03	$[0, 0.5, 1]$	$[0.5\alpha, 1-0.5\alpha], \alpha \in [0\ ,1]$

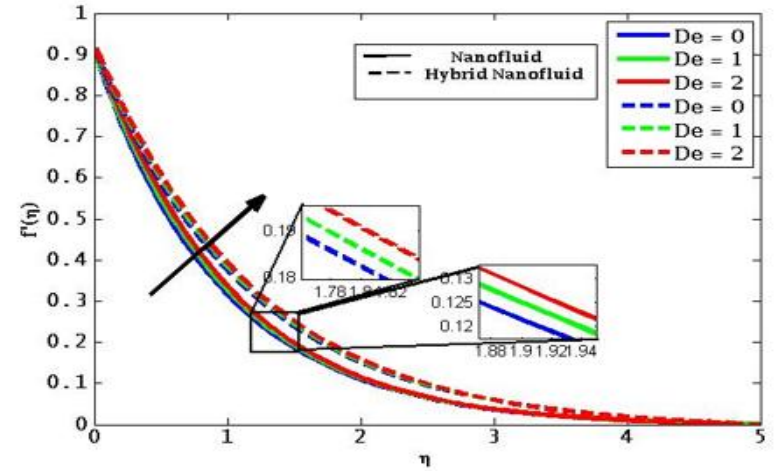

(a)

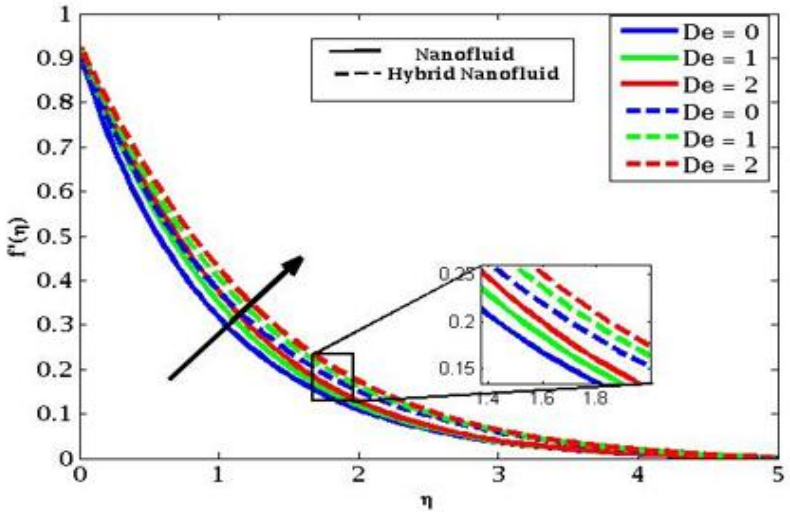

(b)

Figure 3. Velocity effect on De at (a) $n < 1$ and (b) $n > 1$

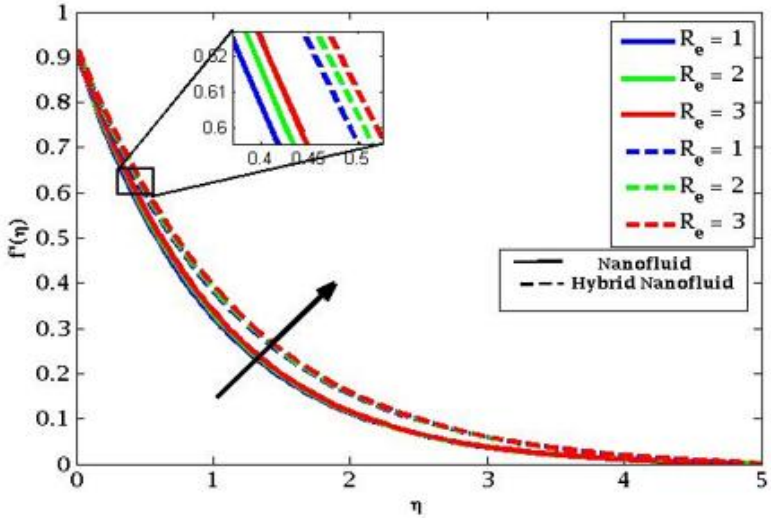

(a)

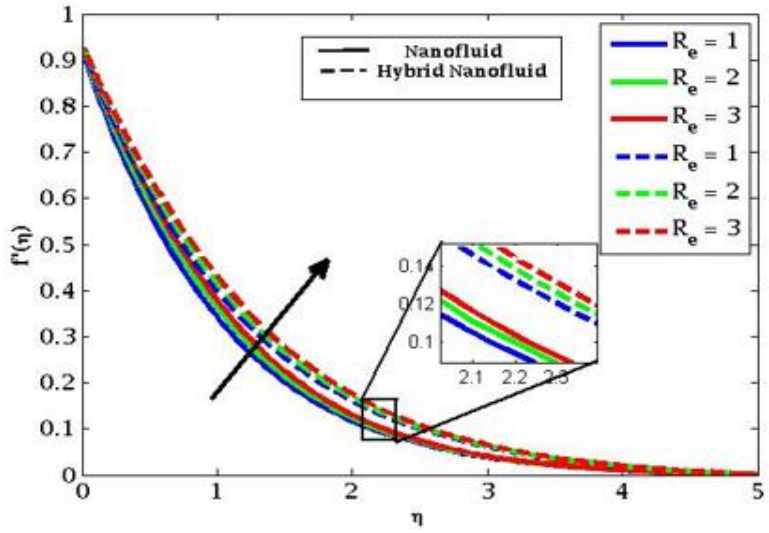

(b)

Figure 4. Velocity effect on $\boldsymbol{Re}$ at (a) $\boldsymbol{n < 1}$ and (b) $\boldsymbol{n > 1}$

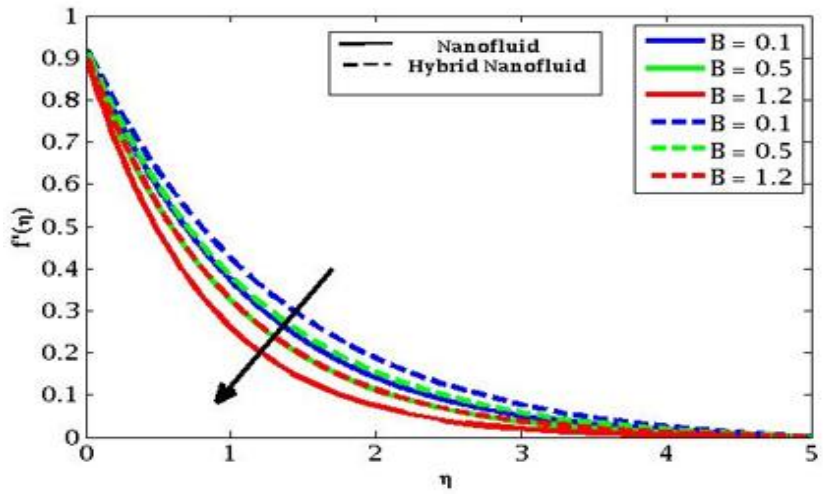

(a)

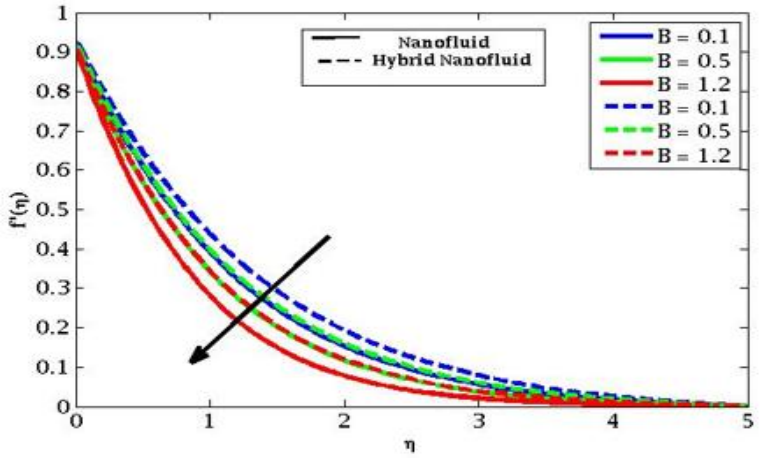

(b)

Figure 5. Velocity effect on B at (a) $n < 1$ and (b) $n > 1$

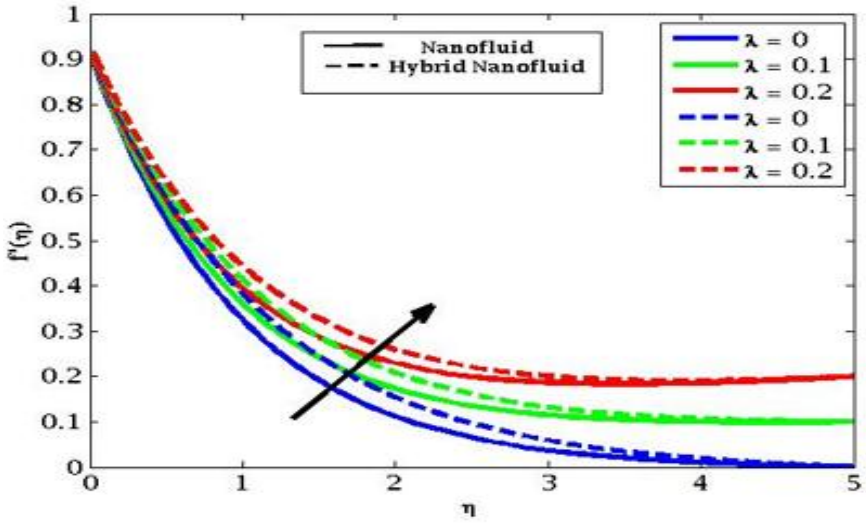

(a)

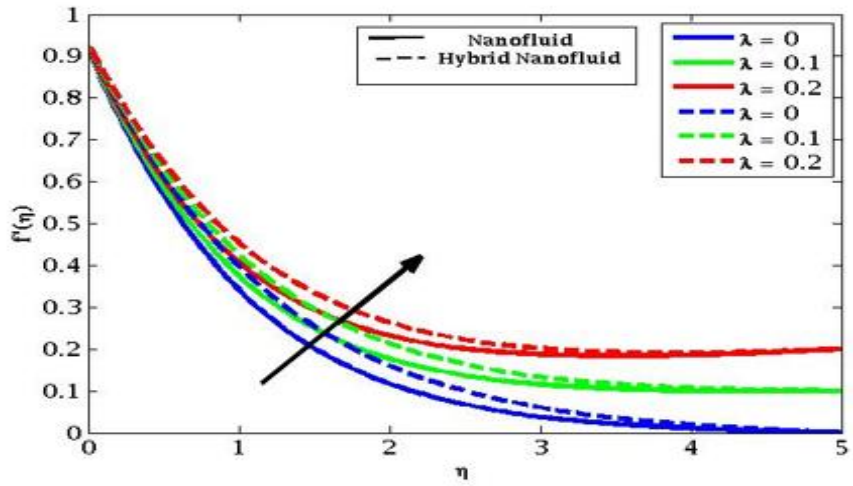

(b)

Figure 6. Velocity effect on λ at (a) $n < 1$ and (b) $n > 1$

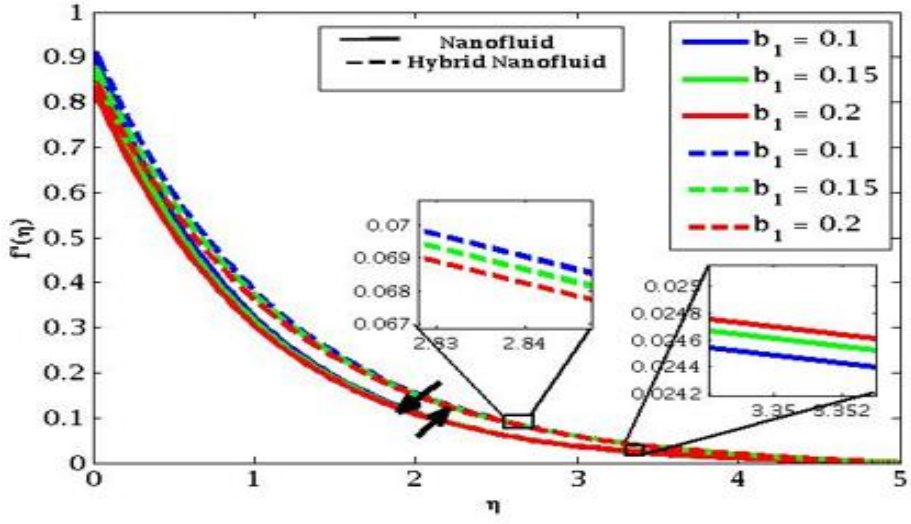

(a)

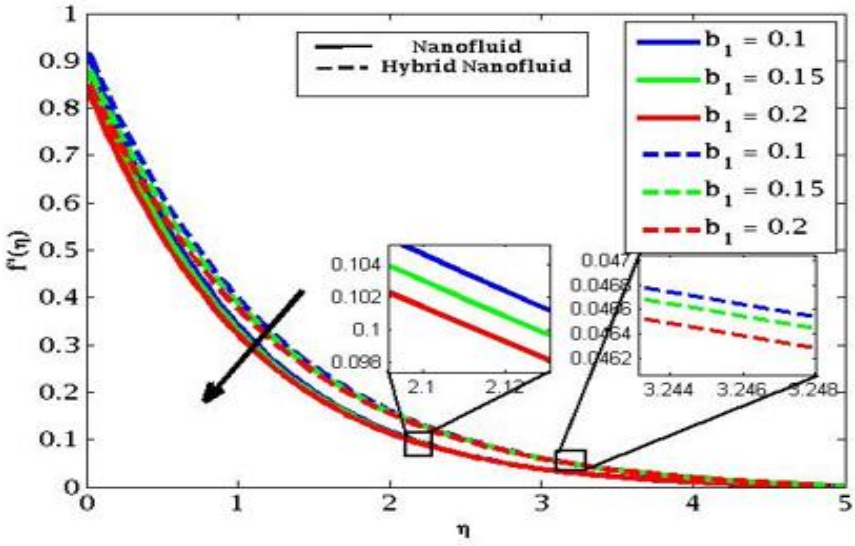

(b)

Figure 7. Velocity effect on b_1 at (a) $n < 1$ and (b) $n > 1$

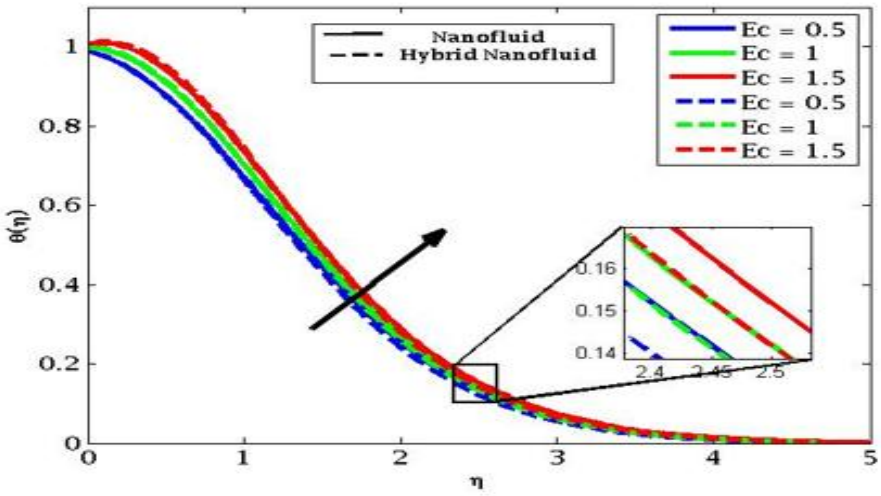

(a)

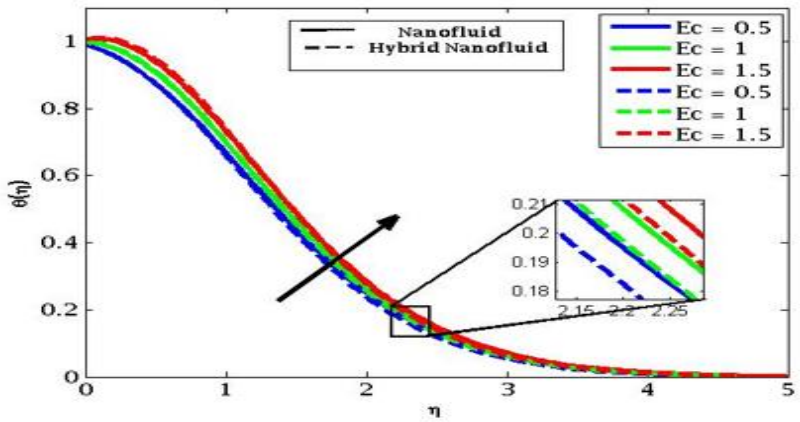

(b)

Figure 8. Temperature effect on Ec at (a) $n < 1$ and (b) $n > 1$

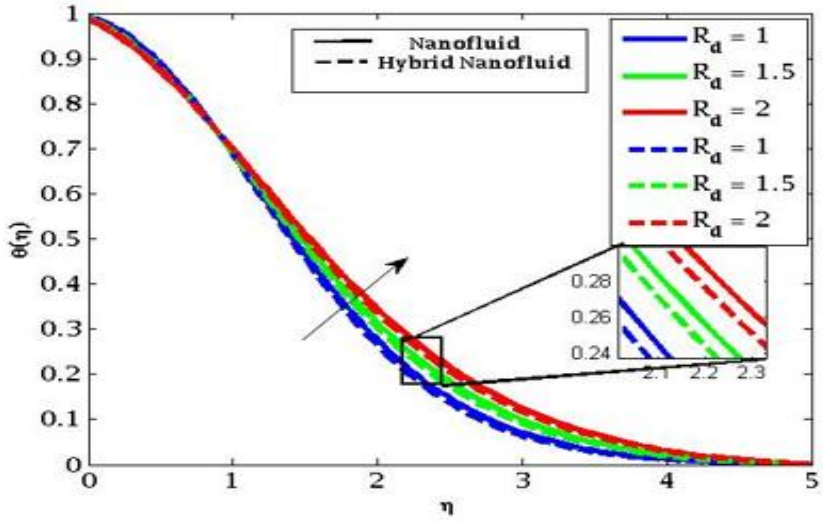

(a)

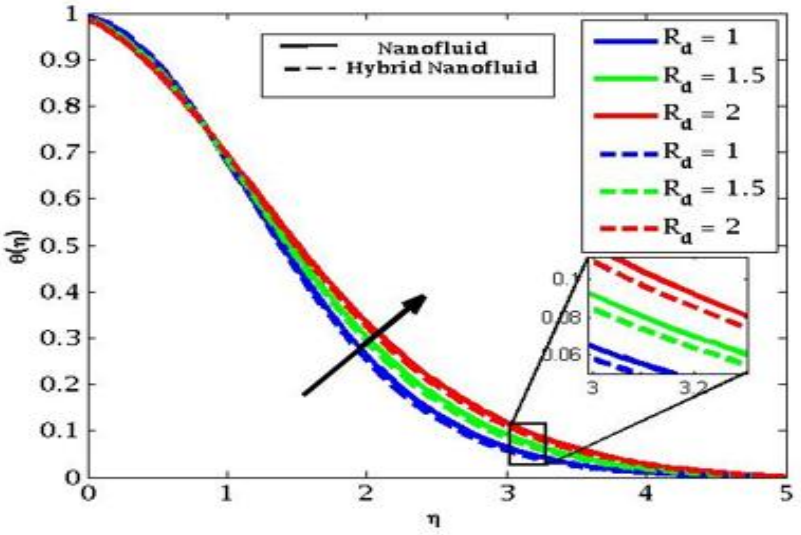

(b)

Figure 9. Temperature effect on R_d at (a) $n < 1$ and (b) $n > 1$

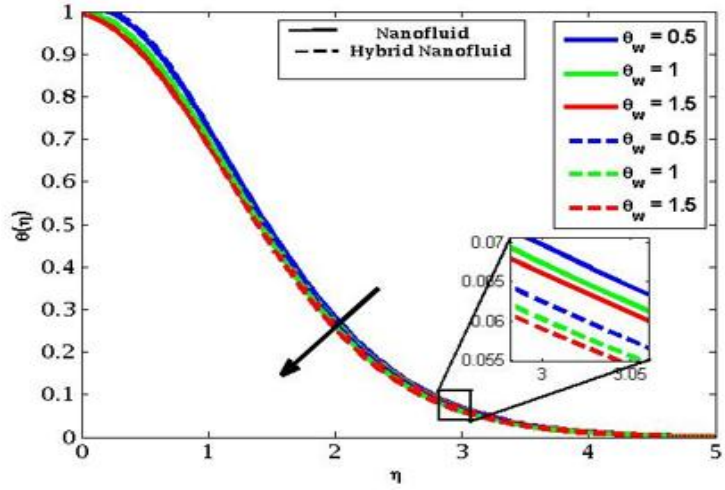

(a)

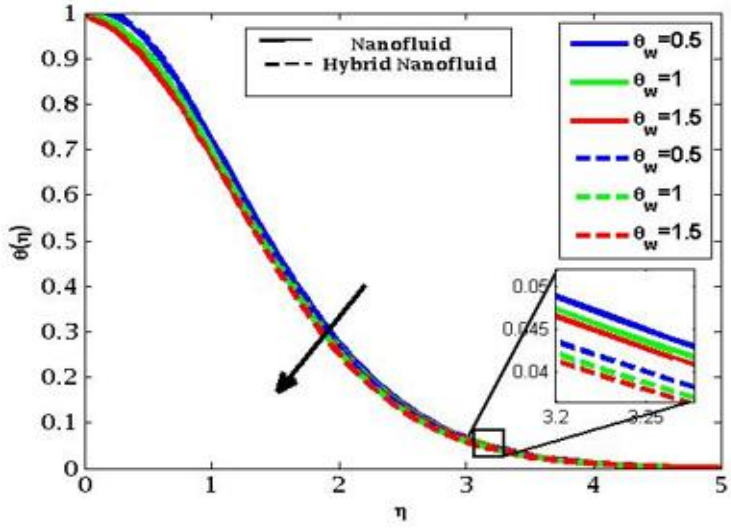

(b)

Figure 10. Temperature effect on θ_w at (a) $n < 1$ and (b) $n > 1$

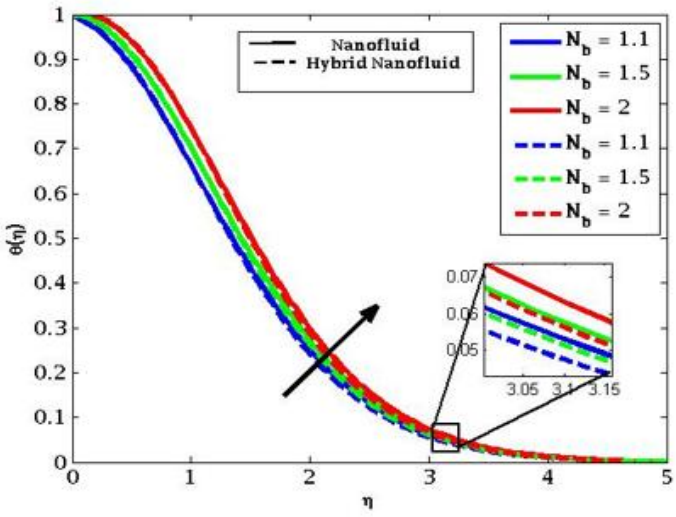

(a)

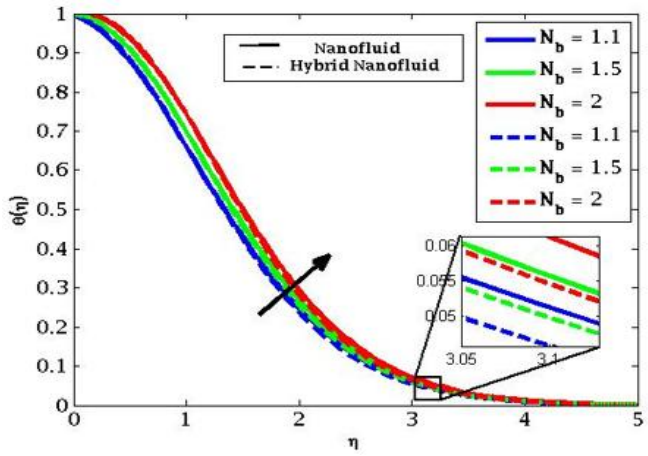

(b)

Figure 11. Temperature effect on N_b at (a) $n < 1$ and (b) $n > 1$

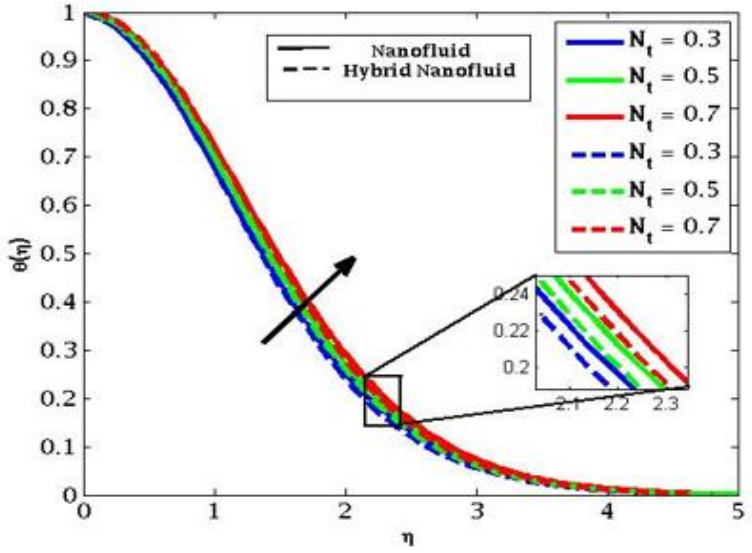

(a)

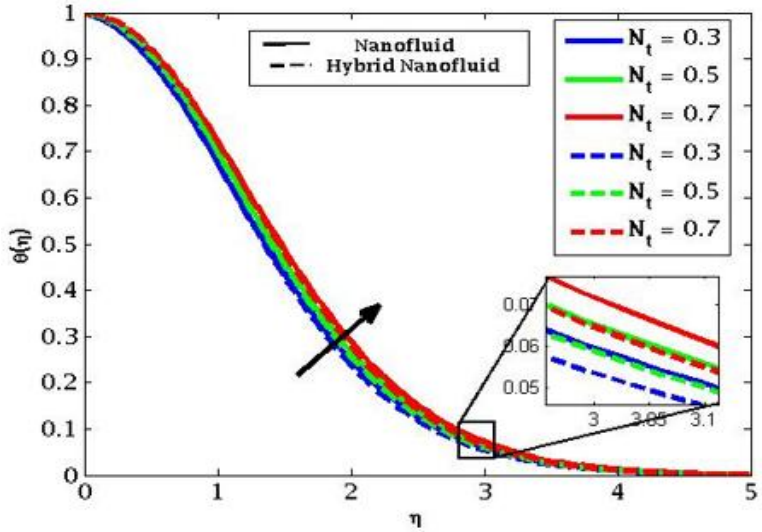

(b)

Figure 12. Temperature effect on N_t at (a) $n < 1$ and (b) $n > 1$

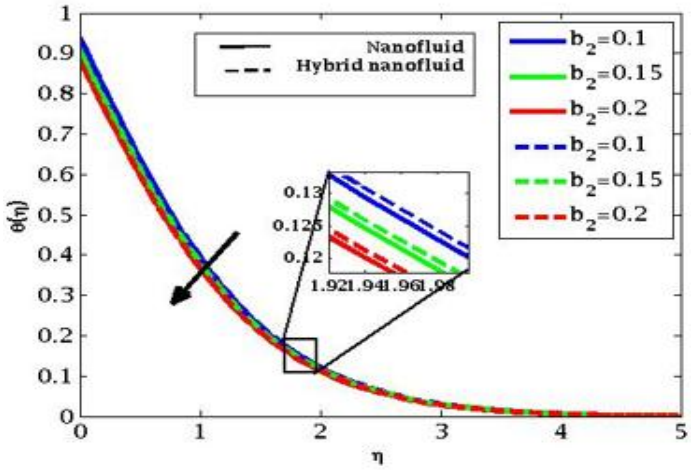

(a)

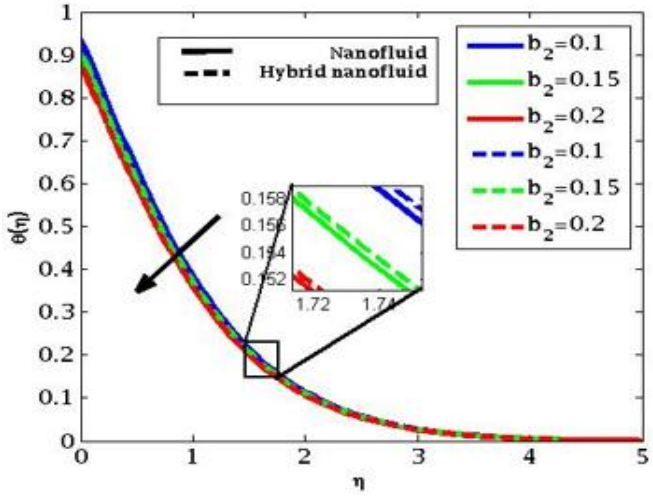

(b)

Figure 13. Temperature effect on b_2 at (a) $n < 1$ and (b) $n > 1$

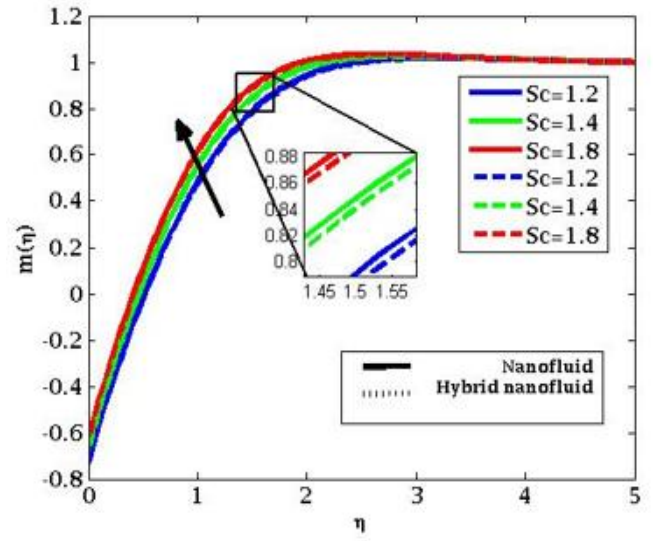

(a)

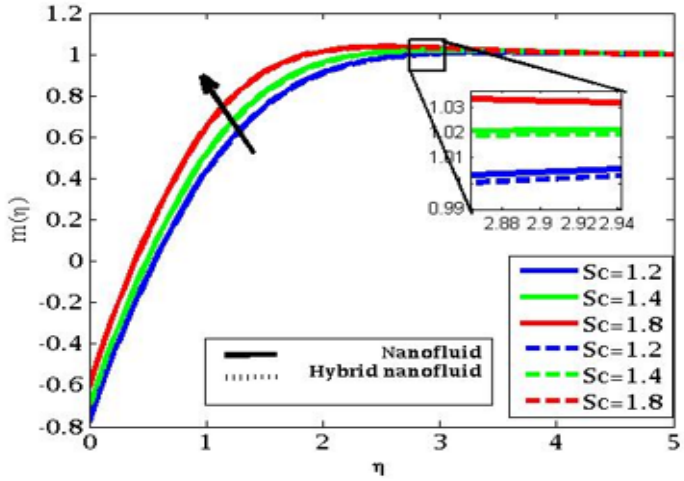

(b)

Figure 14. Concentration effect on Sc at (a) $n < 1$ and (b) $n > 1$

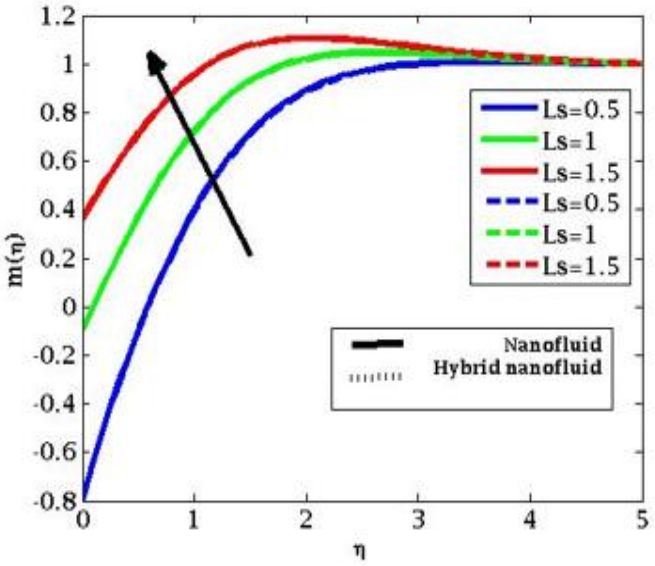

(a)

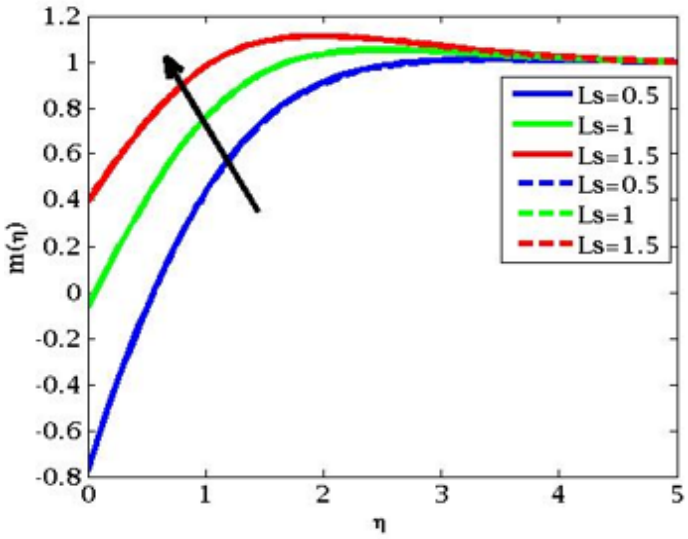

(b)

Figure 15. Concentration effect on Ls at (a) $n < 1$ and (b) $n > 1$

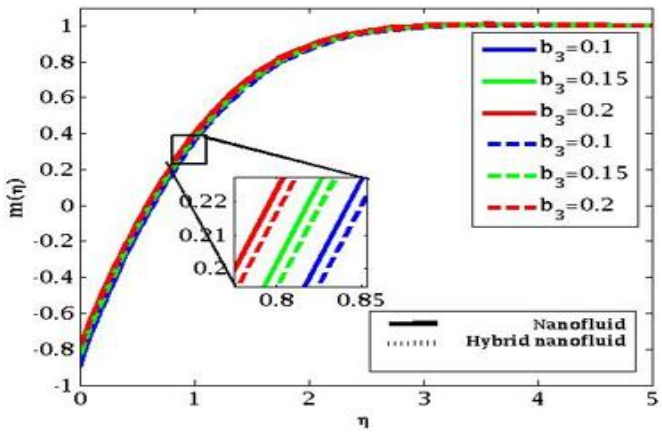

(a)

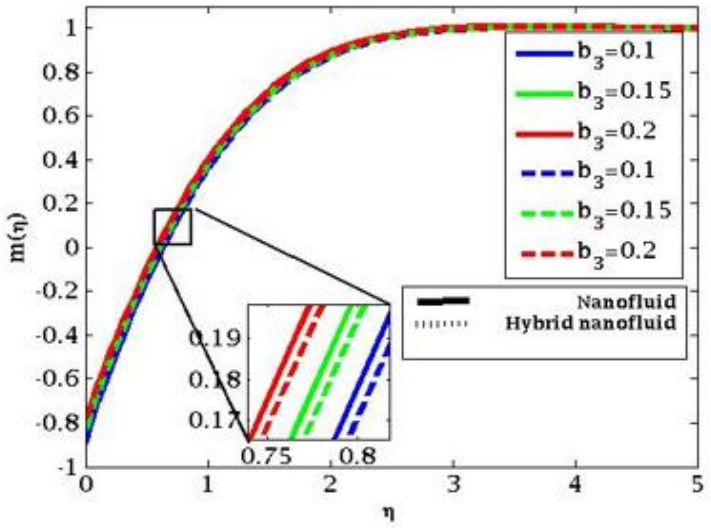

(b)

Figure 16. Concentration effect on b_3 at (a) $n < 1$ and (b) $n > 1$

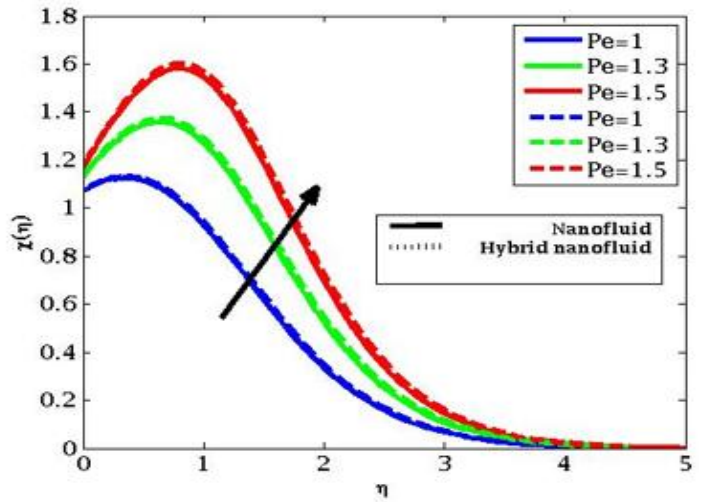

(a)

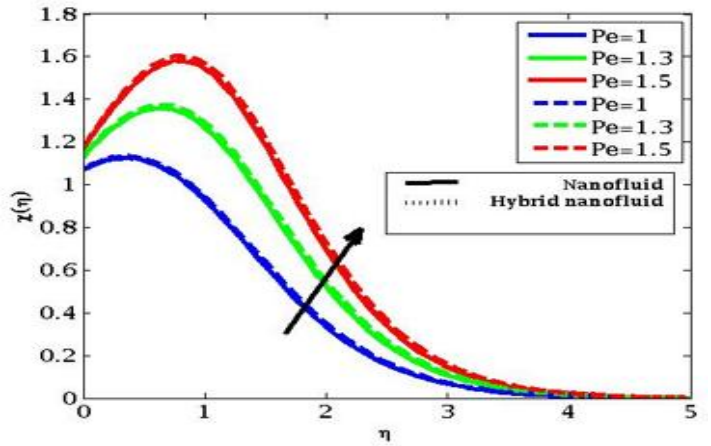

(b)

Figure 17. Microorganism effect on Pe at (a) $n < 1$ and (b) $n > 1$

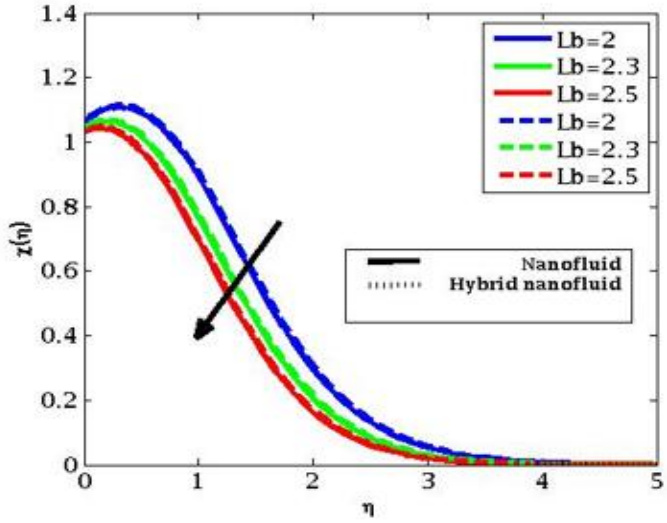

(a)

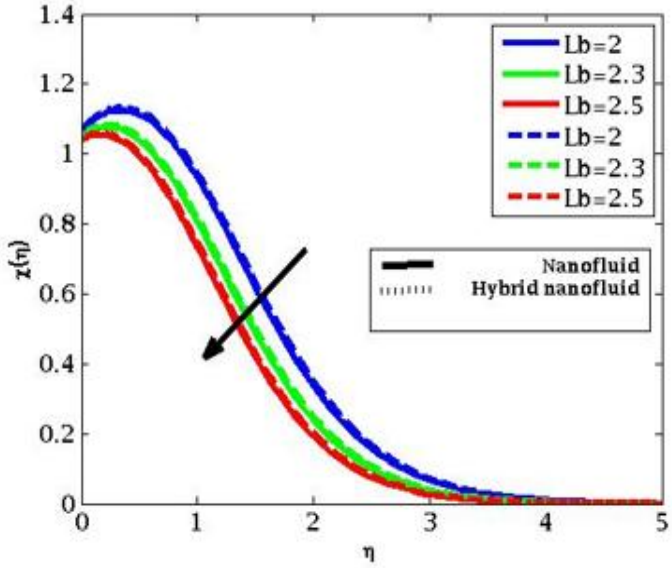

(b)

Figure 18. Microorganism effect on Lb at (a) $n < 1$ and (b) $n > 1$

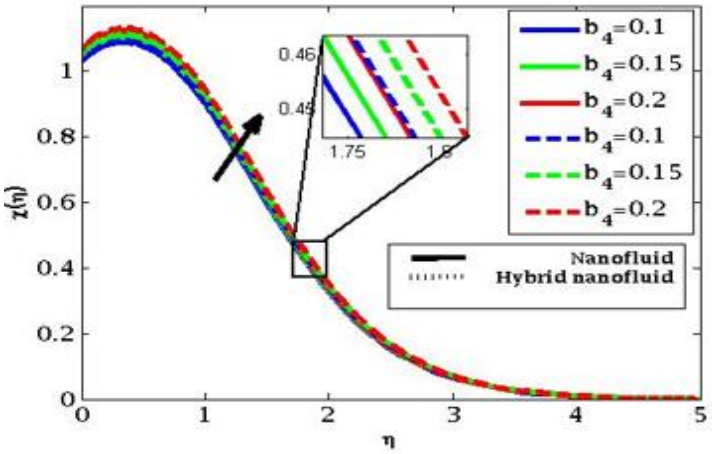

(a)

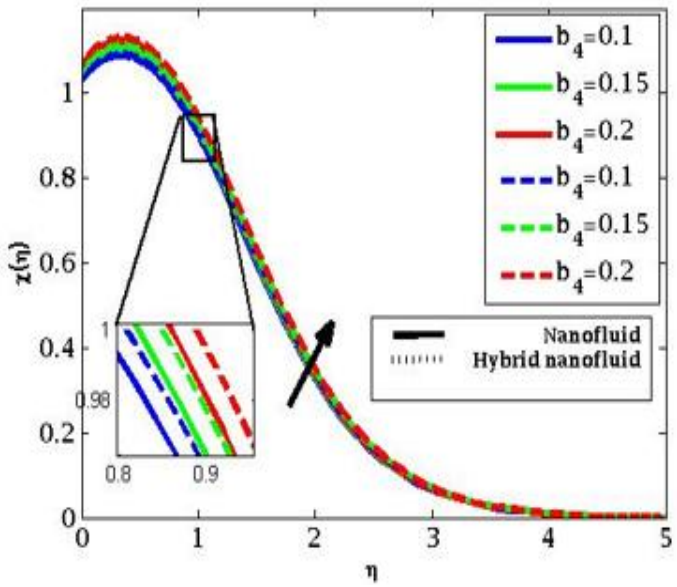

(b)

Figure 19. Microorganism effect on b_4 at (a) $n < 1$ and (b) $n > 1$

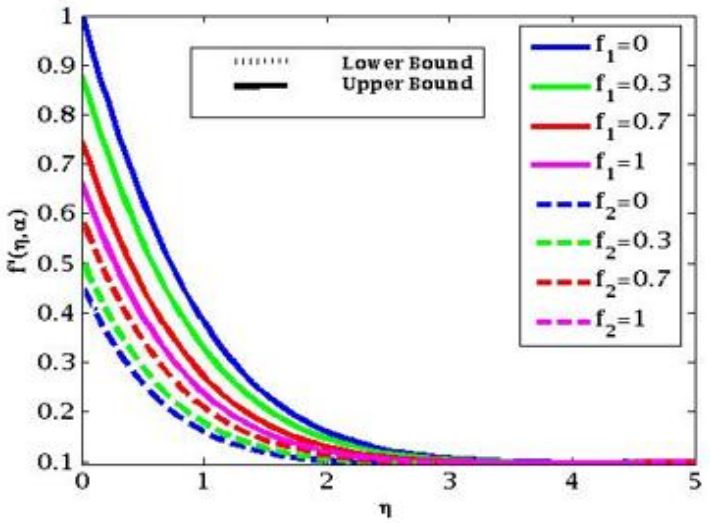

Figure 20. Fuzzy Velocity on hybrid nanofluid

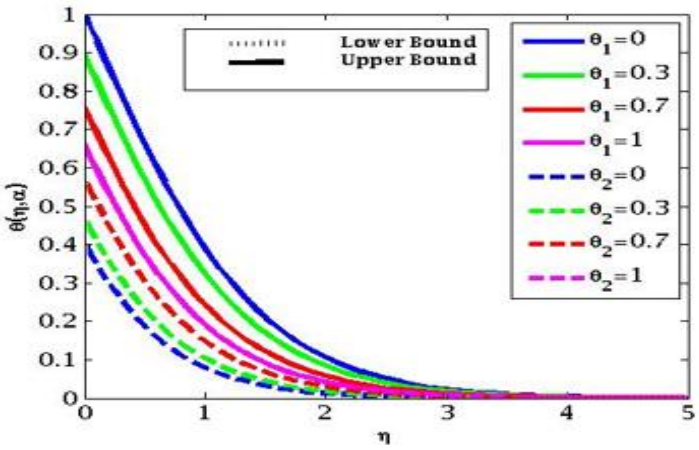

Figure 21. Fuzzy Temperature on hybrid nanofluid

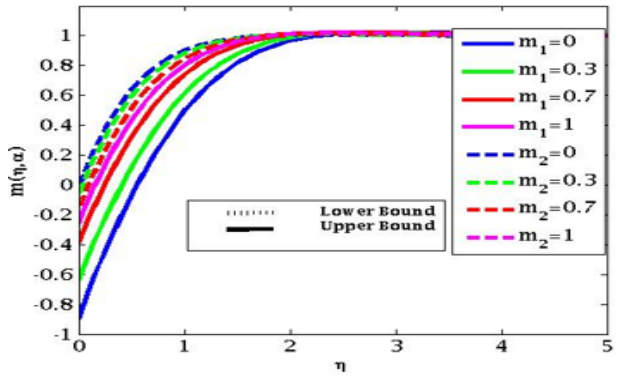

Figure 22. Fuzzy Concentration on hybrid nanofluid

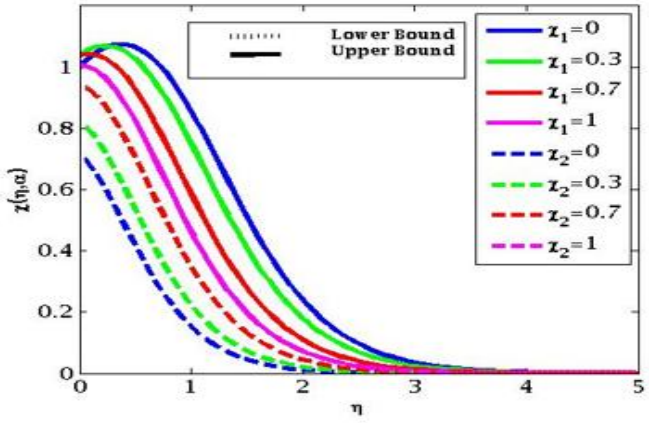

Figure 23. Fuzzy Microorganism on hybrid nanofluid

RESULTS AND DISCUSSION

Velocity Profile

A strong influence of Deborah parameter (D_e), Renolds number (R_e), Magnetic field parameter (B_0), velocity ratio (λ), velocity slip boundary (b_1) parameter on velocity of fluid flow for nanofluid and hybrid nanofluid considering both the characteristics of shear thinning ($n < 1$) and shear thickening ($n > 1$) properties. Figure. 3(a) and (b) demonstrates that in divergent circumstances, the elasticity of nanofluids and hybrid nanofluids is improved with increasing Deborah number (D_e) as a result of longer retardation times. The fluid's velocity increases because its effective viscosity decreases due to its enhanced elasticity. The enhanced elasticity allows for faster velocities in nanofluids and hybrid nanofluids, which in turn allows for more efficient heat dissipation from the stretching sheet. Figure.4(a) and (b) shows that raising the Reynolds number typically causes the fluid velocity to increase. This occurs because the fluid is able to flow with more freedom and speed at higher Reynolds numbers, which indicate a greater ratio of inertial forces to viscous forces. Understanding how R_e affects fluid flow is essential for improving treatment results, guaranteeing accurate medication administration, and controlling heat transfer throughout different organs. Figure.5(a) and (b) illustrates how an electrically conducting fluid encounters a Lorentz force that acts as a resistance to its velocity when subjected to a magnetic field (B_0). The Lorentz force, which acts as an effective opposition to the fluid's motion, becomes stronger with increasing magnetic field intensity, leading to a decrease in the fluid's velocity profile. As the strength of the magnetic field increases, the resistive impact of hybrid nanofluids becomes increasingly more pronounced. Figure.6(a) and (b) demonstrates that when the velocity ratio (λ) is smaller than 1, increasing λ causes the fluid flow velocity to increase. By encouraging a greater flow rate, the velocity relation factor improves the velocity profile even further, particularly in hybrid nanofluids. Managing thermal radiation and the velocity increases with higher λ values, which contribute to greater flow displacement. Figure.7(a) and (b) indicates that velocity slip boundary (b_1) controls particle movement in fluid flow. This relative velocity decays to zero in steady flows and converges to a slow, stable trajectory in turbulent flows. Increased slip boundary (b_1) reduces the velocity profile,

reducing skin friction, heat transmission, and mass transfer. An increased thermal slip parameter decreases heat and mass transfer rates. Slip parameters can influence hybrid nanofluid velocity and transfer qualities to maximize radiation dissipation by managing heat and mass transfer.

Temperature Profile

The impact of Eckert number parameter (Ec), Radiation parameter (R_d), Temperature ratio parameter (θ_w), Brownian motion (Nb), Thermophoresis (Nt) parameter, Thermal slip boundary (b_2) on the temperature of Sutterby fluid flow for nanofluid and hybrid nanofluid considering both the characteristics of shear thinning ($n < 1$) and shear thickening ($n > 1$) properties. Figure.8 (a) and (b) shows that the Eckert number (Ec) greatly affects fluid flow temperature profiles, notably in nanofluids and hybrids. A rise in Eckert number (Ec) indicates more fluid kinetic energy, which increases particle collisions and vibrational energy transfer. This increased collision rate raises boundary layer heat dissipation, raising the temperature profile. An increased Eckert number (Ec) increases fluid friction, causing particles to collide more often and generate thermal energy in the medium. Thus, this dissipation parameter increases thermal boundary layer thickness. Controlling thermal boundary layer thickness and temperature elevation is key to lowering thermal radiation and improving our model's thermal management. Figure. 9(a) and (b) illustrated the radiation parameter (R_d) causes the thermal boundary layer to rise, enhancing the temperature profile in fluid flow. Nanofluids and hybrid nanofluids have enhanced radiative properties like absorption and scattering due to nanoparticles. Increased radiation parameter (R_d) enhances the thermal boundary layer, raising surface temperature. This parameter controls thermal boundary layer formation, which is essential for heat dissipation. Figure. 10 (a) and (b) indicates that increasing the temperature ratio parameter (θ_w) in a nanofluid increases temperature and boundary layer thickness, intensifying its thermal state. Enhanced Brownian motion and thermophoresis increase heat transfer but make it more difficult to control thermal radiation effects on the stretching sheet. However, raising θ_w greatly enhances temperature management in the hybrid nanofluid boundary layer. Multiple nanoparticles improve thermal conductivity and stability, reducing radiative heat effects more effectively. Figure. 11 (a) and (b) illustrates that Brownian motion, driven by the temperature gradient, improves heat transmission by moving nanoparticles in the fluid. In nanofluids with one nanoparticle type, the Brownian motion parameter (Nb) increases thermal energy distribution. The temperature gradient lessens when the thermal boundary layer grows, often due to thermal radiation or MHD effects, limiting nanoparticle mobility. Reduced Brownian motion parameter (Nb) reduces heat transfer. In hybrid nanofluids, synergistic effects initially enhance Brownian motion, but as the boundary layer expands, the lowered temperature gradient reduces its efficiency, lowering heat transfer performance. Figure. 12 (a) and (b) shows that increasing the thermophoresis parameter (Nt) increases the fluid temperature gradient, which increases nanoparticle thermophoretic force. This increased force heats more fluid as nanoparticles move in response to the temperature differential, raising the temperature. Increased nanoparticle concentration improves heat transfer by strengthening the thermophoretic action. Thus, as the thermophoresis parameter (Nt) rises, nanofluid and hybrid nanofluid temperature profiles climb. By modifying Nt, the temperature gradient can be regulated and thermophoretic effects improved, improving stretched sheet thermal management. This will improve heat dissipation, minimizing thermal radiation on the skin and improving our model's thermal effects control. Figure. 13 (a) and (b) emphasized how thermal slip parameter (b_2) affects temperature. The temperature drops as the thermal slip factor increases values. Slip factor (b_2) rises, so lower heat near the surface. Slip essentially causes the fluid to have a loosening of the boundary conditions, so enabling more freedom in its interaction with the solid surface. This then affects the heat transfer process, thereby probably lowering the temperature profile since heat is more easily moved away from the solid boundary.

Concentration Profile

The effects of Schmidt number (Sc), homogenous-heterogenous parameter (Ls), and concentration slip parameter (b_3) on the concentration profile of the nanofluid and hybrid nanofluid considering both the characteristics of shear thinning ($n < 1$) and shear thickening ($n > 1$) properties. Figure. 14 (a) and (b) shows that when the Schmidt number (Sc) grows, turbulent diffusivity drops, lowering fluid concentration and increasing concentration gradient. Higher Scvalues in nanofluids and hybrid

nanofluids diminish mass diffusivity, decreasing concentration more. Higher Schmidt numbers accelerate concentration reduction, highlighting this impact. Reduced mass diffusivity slows nanoparticle and solute dispersion as Scincreases, affecting heat and mass transport. The hybrid nanofluid's mass transfer characteristics can be enhanced by adjusting Sc, improving concentration gradient control and thermal management around the stretched sheet. Controlling Sc optimizes hybrid nanofluid mass transport, improving concentration gradient control and heat management surrounding the stretching sheet. Figure. 15 (a) and (b) shows that homogeneous and heterogeneous parameters (Ls) affect nanofluid and hybrid nanofluid concentration distribution in fluid flows. In homogeneous reactions, especially MHD stagnation point flows, increasing reaction rates thickens the concentration boundary layer. Within the boundary, concentration distribution increases. However, increasing the reaction rate in heterogeneous reactions like MHD flow over a stretching cylinder lowers the concentration profile, especially near the surface. In hybrid nanofluids, heterogeneous reactions increase concentration gradient and homogeneous reactions decrease concentration distribution. Control the concentration profile, optimize mass transfer, and improve thermal regulation by fine-tuning homogeneous and heterogeneous reaction rates. Figure. 16 (a) and (b) depicts how the fluid concentration in both nanofluids and hybrid nanofluids is largely determined by the slip concentration parameter (b_3). Because it restricts particle-fluid interaction close to the boundary layer, a rise in the slip concentration parameter (b_3)lowers the fluid concentration. Our goal is to efficiently regulate fluid concentration by adjusting this parameter, which will maximize heat and mass transmission and reduce thermal radiation.

Microorganism Profile

Figure. 17 (a) and (b) shows the important effect of the Peclet number (Pe) on the gyrotactic microbe profile in hybrid and nanofluids. Pe increases cause the concentration of motile bacteria to rise, hence extending the bioconvection range. This happens since advective transport takes center stage over diffusive transport, accumulating microorganisms in particular flow areas. Although this effect is modest in nanofluids, hybrid nanofluids show a more noticeable rise because of their improved thermal and mass transfer characteristics, hence producing a larger motile boundary layer. Figure. 18 (a) and (b) depicts that the motile microorganism concentration reduces in both nanofluids and hybrid nanofluids as the bioconvection Lewis number (Lb) increases. Reduced mass diffusivity limits the movement and dispersion of microorganisms inside the fluid, thereby causing this reduction. Multiple nanoparticles enhance this effect in hybrid nanofluids by means of their complicated interactions with motile microorganisms, hence causing a sharper drop in microorganism concentration. Optimizing the Lewis number in hybrid nanofluids helps the bandage system to control microorganism distribution, therefore guaranteeing a stable regeneration environment. Figure. 19 (a) and (b) illustrate the microorganisms slip boundary conditions (b_4) affect the behavior of microorganism's profile and the fluid flow itself in both nanofluids and hybrid nanofluid. Microorganisms can increase flow by increasing drag and modifying velocity profile, especially in slip circumstances. Slip can lessen drag and increase velocity, allowing a non-zero velocity near the boundary and affecting microbe behavior.

Fuzzification Profile

The previous section graphically represented the effect of velocity, temperature, concentration, and microorganisms on the crisp value profiles. In this section, it has been discussed how to determine the optimal value of profiles by employing parameters within a range by using fuzzy numbers. The fuzzy framework of various parameters enables the modelling of the most precise and patient specific drug design that is the most efficient dose both functionally and economically. Figure. 20 depicts the effect of fuzzy volume fraction on the velocity of the Sutterby hybrid nanofluid. The $f'(\eta,\alpha)$ represents the velocity profile with upper and lower boundary values of $f_1(\eta,\alpha)$ and $f_2(\eta,\alpha)$ respectively. The α-cut values used for the mathematical model are 0, 0.3, 0.7, 1. The optimized value is found between this range and the velocity becomes consistent and the lines coincide at $\alpha = 1$. Figure. 21 shows the impact of fuzzy volume fraction on the temperature of the Sutterby hybrid nanofluid. The $\theta(\eta,\alpha)$ represents the temperature profile with $\theta_1(\eta,\alpha)$ and $\theta_2(\eta,\alpha)$ as the upper boundary and lower boundary value respectively. An optimized value is found by using the fuzzy concept within the considered small range of α-cut values. The concentration becomes consistent at $\alpha = 1$. Figure. 22 depicts the impact of the

fuzzy volume fraction on the concentration profile of the Sutterby hybrid nanofluid. The $m(\eta,\alpha)$ shows the variation in concentration within the range of α-cut values. The predetermined α-cut values (0, 0.3, 0.7, 1) are analysed between the upper $m_1\,(\eta,\alpha)$ and lower $m_2\,(\eta,\alpha)$ boundaries to find the optimized value. The lines coincide at $\alpha = 1$. Figure. 23 shows the effect of the fuzzy volu.me fraction on the microorganism concentration profile of the Sutterby hybrid nanofluid. The $\chi(\eta,\alpha)$ shows the difference in microorganism concentration within the upper boundary $\chi_1\,(\eta,\alpha)$ and lower boundary $\chi_2\,(\eta,\alpha)$ values. The optimized value is found within the small range of α-cut values and the lines coincide at $\alpha = 1$.

Table 3. Fuzzy velocity profile when $\boldsymbol{R_d = 1, \theta_w = 2, Ec = 0.2, Pr = 2, Sc = 1.2, L_s = 0.5, Lb = 2}$, and $\boldsymbol{Pe = 1}$.

$\boldsymbol{\alpha - cut}$	$\boldsymbol{\lambda}$	$\boldsymbol{De}$	$\boldsymbol{Re}$	$\boldsymbol{B}$	$\boldsymbol{f'(\eta,\alpha)}$							
					$\boldsymbol{n<1}$				$\boldsymbol{n>1}$			
					Nanofluid $\boldsymbol{\varphi_1 = 0.03, \varphi_2 = 0}$		**Hybrid nanofluid** $\boldsymbol{\varphi_1, \varphi_2 = 0.03}$		**Nanofluid** $\boldsymbol{\varphi_1 = 0.3, \varphi_2 = 0}$		**Hybrid nanofluid** $\boldsymbol{\varphi_1, \varphi_2 = 0.03}$	
					$\underline{f'}$	$\bar{f}'$	$\underline{f'}$	$\bar{f}'$	$\underline{f'}$	$\bar{f}'$	$\underline{f'}$	$\bar{f}'$
0.3	0.2	1	1	0.5	0.5095	0.8614	0.4955	0.8568	0.5178	0.8698	0.5043	0.8658
			1.5		0.5112	0.8634	0.4974	0.8590	0.5230	0.8740	0.5099	0.8703
			2		0.5129	0.8652	0.4992	0.8609	0.5279	0.8775	0.5150	0.8740
	0.5	1.5	1	0.3	0.5835	0.8813	0.5659	0.5659	0.5911	0.8890	0.5742	0.8838
				0.5	0.5909	0.8805	0.5736	0.8748	0.5978	0.8883	0.5813	0.8834
				0.7	0.5963	0.8796	0.5796	0.8742	0.6029	0.8875	0.5868	0.8829
0.7	0.2	2	1		0.5845	0.7297	0.5723	0.7215	0.6017	0.7475	0.5906	0.7404
			1.5		0.5819	0.7275	0.5714	0.7207	0.6052	0.7509	0.5959	0.7452
			2		0.5857	0.7316	0.5753	0.7249	0.6135	0.7583	0.6046	0.7529
1	0.5	2	2	0.5	0.7060	0.7060	0.6931	0.6931	0.7254	0.7254	0.7144	0.7144

Table 4. Fuzzy Temperature profile when $\boldsymbol{B_0 = 0.5, \lambda = 0.2, De = 1, Re = 1, Sc = 1.2, L_s = 0.5, Lb = 2}$, and $\boldsymbol{Pe = 1}$.

$\boldsymbol{\alpha - cut}$	$\boldsymbol{R_d}$	$\boldsymbol{\theta_w}$	$\boldsymbol{Ec}$	$\boldsymbol{Pr}$	$\boldsymbol{\theta(\eta,\alpha)}$							
					$\boldsymbol{n<1}$				$\boldsymbol{n>1}$			
					Nanofluid $\boldsymbol{\varphi_1 = 0.03, \varphi_2 = 0}$		**Hybrid nanofluid** $\boldsymbol{\varphi_1, \varphi_2 = 0.03}$		**Nanofluid** $\boldsymbol{\varphi_1 = 0.3, \varphi_2 = 0}$		**Hybrid nanofluid** $\boldsymbol{\varphi_1, \varphi_2 = 0.03}$	
					$\underline{f'}$	$\bar{f}'$	$\underline{f'}$	$\bar{f}'$	$\underline{f'}$	$\bar{f}'$	$\underline{f'}$	$\bar{f}'$
0.3	1	2	0.2	2	0.6257	0.6902	0.6261	0.6952	0.6261	0.6955	0.6266	0.7007
		2.5			0.6242	0.6820	0.6247	0.6864	0.6247	0.6871	0.6252	0.6918
		3			0.6228	0.6744	0.6232	0.6783	0.6233	0.6795	0.6238	0.6836
			0.3		0.6190	0.6576	0.6204	0.6656	0.6194	0.6628	0.6209	0.6712
			0.5	2	0.6114	0.6245	0.6147	0.6405	0.6116	0.6300	0.6150	0.6464
				3	0.7096	0.7630	0.7144	0.7879	0.7096	0.7699	0.7145	0.7950
				4	0.7750	0.8631	0.7807	0.8956	0.7748	0.8712	0.7807	0.9039
0.7	2	2	0.2	2	0.5384	0.5467	0.5382	0.5472	0.5395	0.5493	0.5394	0.5501
		2.5			0.5336	0.5385	0.5332	0.5388	0.5347	0.5411	0.5345	0.5416
		3	0.2		0.5310	0.5289	0.5285	0.5310	0.5301	0.5336	0.5297	0.5339
			0.3	2	0.5246	0.5237	0.5253	0.5255	0.5257	0.5262	0.5264	0.5283
				3	0.6446	0.6587	0.6468	0.6630	0.6456	0.6615	0.6479	0.6661
1	3	2	0.2	2	0.4620	0.4620	0.4615	0.4615	0.4636	0.4636	0.4632	0.4632

Table 5. Fuzzy Concentration profile when $B_0 = 0.5, \lambda = 0.2, De = 1, Re = 1,$ when $R_d = 1, \theta_w = 2, Ec = 0.2, Pr = 2, Lb = 2,$ and $Pe = 1$

$\alpha - cut$	Sc	Ls	$m(\eta, \alpha)$							
			$n < 1$				$n > 1$			
			Nanofluid $\varphi_1 = 0.03$, $\varphi_2 = 0$		**Hybrid nanofluid $\varphi_1, \varphi_2 = 0.03$**		**Nanofluid $\varphi_1 = 0.3$, $\varphi_2 = 0$**		**Hybrid nanofluid $\varphi_1, \varphi_2 = 0.03$**	
			$\underline{f'}$	$\overline{f'}$	$\underline{f'}$	$\overline{f'}$	$\underline{f'}$	$\overline{f'}$	$\underline{f'}$	$\overline{f'}$
0.3	1.2	0.5	1.8828	1.8046	1.8786	1.8036	1.8852	1.8076	1.8811	1.8068
		0.8	1.4991	1.2334	1.4970	1.2332	1.5005	1.2357	1.4985	1.2357
		1	1.3220	1.0278	1.3208	1.0281	1.3230	1.0296	1.3219	1.0300
0.7	1.5	0.5	1.9184	1.8035	1.9147	1.8009	1.9216	1.8079	1.9182	1.8057
		1	1.2796	1.1271	1.2789	1.1270	1.2808	1.1288	1.2802	1.1289
1	1.5	1	1.2024	1.2024	1.2020	1.2020	1.2039	1.2039	1.2036	1.2036

Table 6. Fuzzy Microorganism profile when $B_0 = 0.5, \lambda = 0.2, De = 1, Re = 1,$ when $R_d = 1, \theta_w = 2, Ec = 0.2, Pr = 2.$

$\alpha - cut$	Lb	Pe	$\chi(\eta, \alpha)$							
			$n < 1$				$n > 1$			
			Nanofluid $\varphi_1 = 0.03$, $\varphi_2 = 0$		**Hybrid nanofluid $\varphi_1, \varphi_2 = 0.03$**		**Nanofluid $\varphi_1 = 0.3$, $\varphi_2 = 0$**		**Hybrid nanofluid $\varphi_1, \varphi_2 = 0.03$**	
			$\underline{f'}$	$\overline{f'}$	$\underline{f'}$	$\overline{f'}$	$\underline{f'}$	$\overline{f'}$	$\underline{f'}$	$\overline{f'}$
0.3	2	1	0.4480	0.2618	0.4428	0.2486	0.4502	0.2718	0.4451	0.2593
		2	0.8873	0.4018	0.9413	0.4247	0.8679	0.3913	0.9204	0.4132
		3	4.1147	0.9896	3.9830	1.0260	4.1614	0.9822	4.0266	1.0177
0.7	2	1	0.4021	0.3103	0.3941	0.2983	0.4061	0.3182	0.3984	0.3069
		2	0.8377	0.5907	0.8833	0.6202	0.8184	0.5763	0.8625	0.6047
1	3	1	0.6753	0.6753	0.6682	0.6682	0.6800	0.6800	0.6733	0.6733

Table 3 Using fuzzy logic, show the impact of λ, De, Re, B and $\alpha - cut$ on the velocity profiles of hybrid and nanofluids for both shear thinning and shear thickening fluid. It shows that uncertainty (through α-cut) affects the velocity limitations; hybrid nanofluids usually exhibit improved flow behavior. Convergence most certainly occurs at $\alpha = 1$ as the velocity numbers for both fluids seem to be the same.

Table 4 incorporates fuzzy logic to evaluate the effect on the temperature profile of hybrid and nanofluids of $E_c, P_r, R_d, \boldsymbol{\theta_w}$ and $\alpha - cut$ for both shear thinning and shear thickening fluid. It shows that among pure nanofluids; hybrid nanofluids enhance thermal characteristics. Under 100% uncertainty, both liquids display the same temperature readings at $\alpha = 1$, hence they are compatible.

Table 5 presents a fuzzy logic method applied for Sc, Ls and α-cut values for the concentration profile of hybrid nanofluids and nanofluids for both shear thinning and shear thickening fluid. Over several conditions, hybrid nanofluid always shows better concentration properties. At $\alpha = 1$ both liquids show equal values, thereby verifying consistency under complete certainty.

Table 6 presents a fuzzy logic study of L_b, P_e and $\alpha - cut$ on the microorganism profile for hybrid and nanofluids for both shear thinning and shear thickening fluid. Hybrid nanofluids show remarkable concentration performance over the fuzzy range. At $\alpha = 1$, both fluids yield the identical values, indicating agreement under perfect knowledge.

Limitations: While this computational study provides significant insights into the use of MHD Sutterby hybrid nanofluids for solar protection, several limitations remain. First, the mathematical model assumes a steady, two-dimensional flow, which may not fully capture the complexities of unsteady, three-

dimensional physiological fluid dynamics. Second, the study relies on the Rosseland approximation for thermal radiation; however, this approach may oversimplify the non-linear interaction between radiation and biological tissues. Third, while fuzzy logic effectively addresses volume fraction uncertainty, the specific chemical interactions between Cadmium Selenide (CdSe), Chitosan, and human blood components were not chemically modeled. Finally, the research is strictly numerical and theoretical, requiring future experimental validation and clinical trials to confirm the biocompatibility and actual defensive efficacy of these hybrid nanoparticles in living systems.

CONCLUSION

This study concludes that the integration of Sutterby hybrid nanofluid dynamics with fuzzy logic provides a robust framework for managing solar thermal radiation and enhancing skin protection. By utilizing MATLAB to solve the transformed nonlinear governing equations, the research effectively demonstrates how Cadmium Selenide (CdSe) and Chitosan nanoparticles can be optimized to mitigate radiation absorption. The findings reveal that the velocity profile is significantly enhanced by increasing the Deborah number (De), Reynolds number (Re), and slip parameter (b1), whereas the application of a magnetic field (M) exerts a resistive Lorentz force that reduces fluid speed. Statistically, thermal energy distribution is directly proportional to the Eckert number (Ec), thermal radiation parameter (Rd), Brownian motion (Nb), and thermophoresis (Nt), all of which contribute to a thicker thermal boundary layer for both shear-thinning and shear-thickening fluids. Conversely, the temperature ratio (θw) and temperature slip (δ_1) show an inverse relationship with the temperature profile. In the context of bioconvection, the concentration of microorganisms increases with the bioconvective Peclet number (Pe), yet diminishes as the Lewis number (Le) rises. The inclusion of fuzzy analysis using α-cut values confirms that physical results remain stable and consistent at α= 1, bridging the gap between theoretical modeling and imprecise real-world parameters. This methodology demonstrates that fuzzy hybrid nanofluids offer a more reliable defense mechanism than traditional topical treatments. Future research should expand this model to include three-dimensional flow geometries and the effects of unsteady flow conditions to further refine its application in biomedical engineering and solar protection technology.

Data availability

Data sharing not applicable – no new data generated.

Conflicts of Interest

No, there is no conflict of interest

Funding

No funding was received for this research.

Acknowledgments

The authors would like to express their gratitude to Government College Technology, Coimbatore, India.

REFERENCES

[1] Hayat T, Zahir H, Mustafa M, Alsaedi A. Peristaltic flow of Sutterby fluid in a vertical channel with radiative heat transfer and compliant walls: a numerical study. Results in physics. 2016 Jan 1;6:805-10. https://doi.org/10.1016/j.rinp.2016.10.015

[2] Abdul Basit M, Imran M, Khan SA, Alhushaybari A, Sadat R, Ali MR. Partial differential equations modeling of bio-convective sutterby nanofluid flow through paraboloid surface. Scientific Reports. 2023 Apr 15;13(1):6152. https://doi.org/10.1038/s41598-023-32902-z

[3] Sabir Z, Imran A, Umar M, Zeb M, Shoaib M, Raja MA. A numerical approach for 2-D Sutterby fluid-flow bounded at a stagnation point with an inclined magnetic field and thermal radiation impacts. Thermal Science. 2021;25(3 Part A):1975-87. https://doi.org/10.2298/TSCI191207186S

[4] Usman AH, Saeed Khan N, Ali Rano S, Maitama M. Study of heat and mass transfer in MHD flow of sutterby nanofluid over a curved stretching sheet with magnetic dipole and effect. Thai Journal of Mathematics. 2021 Jun 8;19(3):1037-55.

[5] Aldabesh A, Haredy A, Al-Khaled K, Khan SU, Tlili I. Darcy resistance flow of Sutterby nanofluid with microorganisms with applications of nano-biofuel cells. Scientific Reports. 2022 May 7;12(1):7514. https://doi.org/10.1038/s41598-022-11528-7

[6] Zeeshan A, Awais M, Alzahrani F, Shehzad N. Energy analysis of non-Newtonian nanofluid flow over parabola of revolution on the horizontal surface with catalytic chemical reaction. Heat Transfer. 2021 Sep;50(6):6189-209. https://doi.org/10.1002/htj.22168

[7] Haq F, Saleem M, Khan MI. Investigation of mixed convection magnetized Casson nanomaterial flow with activation energy and gyrotactic microorganisms. Journal of Physics Communications. 2021 Dec 2;5(12):125001. https://doi.org/10.1088/2399-6528/ac3889

[8] Punith Gowda RJ, Naveen Kumar R, Jyothi AM, Prasannakumara BC, Sarris IE. Impact of binary chemical reaction and activation energy on heat and mass transfer of marangoni driven boundary layer flow of a non-Newtonian nanofluid. Processes. 2021 Apr 16;9(4):702. https://doi.org/10.3390/pr9040702

[9] Benhanifia K, Redouane F, Lakhdar R, Brahim M, Al-Farhany K, Jamshed W, Eid MR, El Din SM, Raizah Z. Investigation of mixing viscoplastic fluid with a modified anchor impeller inside a cylindrical stirred vessel using Casson–Papanastasiou model. Scientific Reports. 2022 Oct 20;12(1):17534. https://doi.org/10.1038/s41598-022-22415-6

[10] Jamshed W, Eid MR, Al-Hossainy AF, Raizah Z, Tag El Din ES, Sajid T. RETRACTED ARTICLE: Experimental and TDDFT materials simulation of thermal characteristics and entropy optimized of Williamson Cu-methanol and Al2O3-methanol nanofluid flowing through solar collector. Scientific Reports. 2022 Oct 28;12(1):18130. https://doi.org/10.1038/s41598-022-23025-y

[11] Ali B, Hussain S, Nie Y, Ali L, Hassan SU. Finite element simulation of bioconvection and cattaneo-Christov effects on micropolar based nanofluid flow over a vertically stretching sheet. Chinese Journal of Physics. 2020 Dec 1; 68:654-70. https://doi.org/10.1016/j.cjph.2020.10.021

[12] Khan SA, Waqas H, Naqvi SM, Alghamdi M, Al-Mdallal Q. Cattaneo-Christov double diffusions theories with bio-convection in nanofluid flow to enhance the efficiency of nanoparticles diffusion. Case Studies in Thermal Engineering. 2021 Aug 1; 26:101017. https://doi.org/10.1016/j.csite.2021.101017

[13] Hayat T, Ullah I, Muhammad K, Alsaedi A. Gyrotactic microorganism and bio-convection during flow of Prandtl-Eyring nanomaterial. Nonlinear Engineering. 2021 Jan 1;10(1):201-12. https://doi.org/10.1515/nleng-2021-0015

[14] Asjad MI, Zahid M, Jarad F, Alsharif AM. Bioconvection flow of MHD viscous nanofluid in the presence of chemical reaction and activation energy. Mathematical Problems in Engineering. 2022;2022(1):1707894. https://doi.org/10.1155/2022/1707894

[15] Imran M, Kamran T, Khan SA, Muhammad T, Waqas H. Physical attributes of bio-convection in nanofluid flow through a paraboloid of revolution on horizontal surface with motile microorganisms. International Communications in Heat and Mass Transfer. 2022 Apr 1; 133:105947. https://doi.org/10.1016/j.icheatmasstransfer.2022.105947

[16] Freire GF. Federated Learning Models for Privacy-Preserving Healthcare Data Analysis. Journal of Wireless Intelligence and Spectrum Engineering. 2025 Apr 18:19-25.

[17] Awan AU, Shah SA, Ali B. Bio-convection effects on Williamson nanofluid flow with exponential heat source and motile microorganism over a stretching sheet. Chinese Journal of Physics. 2022 Jun 1; 77:2795-810. https://doi.org/10.1016/j.cjph.2022.04.002

[18] Ramesh GK, Madhukesh JK, Aly EH, Pop I. Modified Buongiorno's model for biomagnetic hybrid nanoliquid past a permeable moving thin needle. International Journal of Numerical Methods for Heat & Fluid Flow. 2022 Oct 14;32(11):3551-78. https://doi.org/10.1108/HFF-10-2021-0696

[19] Daniel YS, Aziz ZA, Ismail Z, Salah F. Thermal radiation on unsteady electrical MHD flow of nanofluid over stretching sheet with chemical reaction. Journal of King Saud University-Science. 2019 Oct 1;31(4):804-12.

[20] Venkata KB, Jayaramireddy K, Charankumar G. MHD and thermal radiation effects of a nanofluid over a stretching sheet using HAM. Int. J. Recent Technol. Eng. (IJRTE). 2019;8(4):3489-96.

[21] Dash RK, Mishra SR, Pattnaik PK. Influence of radiative heat energy on the MHD flow of Cu-kerosene nanofluid over a vertical plate: Laplace transform technique. Biointerface Res. Appl. Chem. 2022;12(5):6234-51. https://doi.org/10.33263/BRIAC125.62346251

[22] Sadulla S. Vertical Farming of Spinach Using Renewable Energy-Integrated Smart Growth Modules. National Journal of Plant Sciences and Smart Horticulture. 2023 Dec 16:1-8.

[23] Mondal S, Pal D. Exploring convective entropy optimization and activation energy impact on magneto-nanofluid flow over a vertical stretched plate with Hall current and nonlinear thermal radiation using SQLM. Hybrid Advances. 2024 Dec 1; 7:100294. https://doi.org/10.1016/j.hybadv.2024.100294

[24] Vaidya H, Choudhari R, Mebarek-Oudina F, Animasaun IL, Prasad KV, Makinde OD. Combined effects of homogeneous and heterogeneous reactions on peristalsis of Ree-Eyring liquid: Application in hemodynamic flow. Heat Transfer. 2021 May;50(3):2592-609. https://doi.org/10.1002/htj.21995

[25] Upreti H, Joshi N, Pandey AK, Rawat SK. Homogeneous–heterogeneous reactions within magnetic sisko nanofluid flow through stretching sheet due to convective conditions using Buongiorno's model. Journal of Nanofluids. 2022 Aug 1;11(5):646-56. https://doi.org/10.1166/jon.2022.1875

[26] Haq I, Naveen Kumar R, Gill R, Madhukesh JK, Khan U, Raizah Z, Eldin SM, Boonsatit N, Jirawattanapanit A. Impact of homogeneous and heterogeneous reactions in the presence of hybrid nanofluid flow on various geometries. Frontiers in Chemistry. 2022 Oct 18;10:1032805. https://doi.org/10.3389/fchem.2022.1032805

[27] Ghasemi Moghaddam R, Abbasbandy S, Rostamy-Malkhalifeh M. A S tudy on Analytical Solutions of the Fuzzy Partial Differential Equations. International Journal of Industrial Mathematics. 2020 Aug 1;12(4):419-29.

[28] Moatimid GM, Elgazery NS, Mohamed MA, Elagamy K. Bio-convection flow of Sutterby nanofluid with motile microbes on stretchable sheet: exponentially varying viscosity. Journal of Applied and Computational Mechanics. 2024 Jul 1;10(3):488-502. https://doi.org/10.22055/jacm.2024.45527.4380

[29] Geetha K, Saranya N. Impact of Organic Soil Amendments on Soil Microbial Diversity and Crop Productivity. Journal of Environmental Sustainability, Climate Resilience, and Agro-Ecosystems. 2025 Sep 17;2(2):8-13.

[30] Jameel AF, Ghoreishi M, Ismail AI. Approximate solution of high order fuzzy initial value problems. Journal of uncertain systems. 2014;8(2):149-60.

[31] Barhoi A, Hazarika GC, Dutta P. Numerical study of fuzzified boundary value problem for Couette type flow of fluid mechanics. Annals of Pure and Applied Mathematics. 2018;16(2):373-84. http://dx.doi.org/10.22457/apam.v16n2a14

[32] Biswal U, Chakraverty S, Ojha BK. Natural convection of nanofluid flow between two vertical flat plates with imprecise parameter. Coupled systems mechanics. 2020 Jun;9(3):219-35. https://doi.org/10.12989/csm.2020.9.3.219

[33] Dubois D, Prade H. Operations on fuzzy numbers. International Journal of systems science. 1978 Jun 1;9(6):613-26. https://doi.org/10.1080/00207727808941724

[34] Deepika J. Hardware–Algorithm Co-Design of Adaptive LMS/NLMS Signal Processing Pipelines for Power-Constrained Embedded Systems. National Journal of Integrated VLSI and Signal Intelligence. 2026:26-33.

[35] Seikkala S. On the fuzzy initial value problem. Fuzzy sets and systems. 1987 Dec 1;24(3):319-30. https://doi.org/10.1016/0165-0114(87)90030-3